A High-order Accurate Scheme for Maxwell's Equations with a Generalized Dispersive Material (GDM) Model and Material Interfaces

Jeffrey W. Banks[a,1,3,4], Benjamin B. Buckner[a,1,3], William D. Henshaw[a,1,3,*],
Michael J. Jenkinson[a,1,2], Alexander V. Kildishev[b,1], Gregor Kovačič[a,1], Ludmila J. Prokopeva[b,1],
Donald W. Schwendeman[a,1,3]

[a] *Department of Mathematical Sciences, Rensselaer Polytechnic Institute, Troy, NY 12180, USA*
[b] *School of Electrical and Computer Engineering, Purdue University, West Lafayette, IN 47907, USA*

Abstract

A high-order accurate scheme for solving the time-domain dispersive Maxwell's equations and material interfaces is described. Maxwell's equations are solved in second-order form for the electric field. A generalized dispersive material (GDM) model is used to represent a general class of linear dispersive materials and this model is implemented in the time-domain with the auxiliary differential equation (ADE) approach. The interior updates use our recently developed second-order and fourth-order accurate single-stage three-level space-time finite-difference schemes, and this paper extends these schemes to treat interfaces between different dispersive materials. Composite overlapping grids are used to treat complex geometry with Cartesian grids generally covering most of the domain and local conforming grids representing curved boundaries and interfaces. Compatibility conditions derived from the interface jump conditions and governing equations are used to derive accurate numerical interface conditions that define values at ghost points. Although some compatibility conditions couple the equations for the ghost points in tangential directions due to mixed-derivatives, it is shown how to decouple the equations to avoid solving a larger system of equations for all ghost points on the interface. The stability of the interface approximations is studied with mode analysis and it is shown that the schemes retain close to a *CFL-one* time-step restriction. Numerical results are presented in two and three space dimensions to confirm the accuracy and stability of the schemes. The schemes are verified using exact solutions for a planar interface, a disk in two-dimensions, and a solid sphere in three-dimensions.

Keywords: time-domain electromagnetics; dispersive Maxwell's equations; material interfaces; overlapping grids

---

[*] Corresponding author

Email addresses: `banksj3@rpi.edu` (Jeffrey W. Banks), `bucknb2@rpi.edu` (Benjamin B. Buckner), `henshw@rpi.edu` (William D. Henshaw), `jenkim22@rpi.edu` (Michael J. Jenkinson), `kildishev@purdue.edu` (Alexander V. Kildishev), `kovacg@rpi.edu` (Gregor Kovačič), `lprokop@purdue.edu` (Ludmila J. Prokopeva), `schwed@rpi.edu` (Donald W. Schwendeman)

[1] This work was partially funded by the DARPA Defense Sciences Office, Award HR00111720032.

[2] This work was partially funded by the NSF Research Training Group Grant DMS-1344962.

[3] This work was partially performed under DOE contracts from the ASCR Applied Math Program.

[4] Research supported by a U.S. Presidential Early Career Award for Scientists and Engineers.

Contents

1. Introduction

The accurate numerical modeling of the optical response of an electromagnetic pulse incident on a temporally and spatially dispersive medium (e.g., an optical metamaterial or metasurface) is currently a central and challenging problem in computational nanophotonics. For example, the dynamics of optical pulses propagating in dispersive optical elements is of critical importance in many engineering applications, including fiber and integrated optics [1–3], optical computing [4–6], advanced time-resolved near-field microscopy [7, 8] and nanofocusing [9, 10] systems. Recent progress in using digitally-coded microwave signals for controlling ultrashort optical pulses and employing nanostructured metal-dielectric composites for strong localization of light emphasizes the importance of reducing the influence of numerical dispersion artifacts on the actual causal physical effects of local and non-local temporal dispersion in such systems.

In this article, we address this challenging problem by presenting a unified approach to the numerical modeling of electromagnetic wave propagation in linear, causally dispersive media using a high-order accurate finite-difference time-domain scheme on overset grids with novel boundary conditions at material interfaces. Our approach blends significant contributions in the areas of computational electromagnetics, optical materials science, and numerical analysis. Key algorithms are developed for the field of optics, where temporal dispersion of the dielectric permittivity (electric conductivity) in a piece-wise homogeneous medium is considered, while the magnetic permeability remains constant and equal to that of vacuum. The focus of the current work is on the development, numerical analysis, and verification of novel approximations at material interfaces between dispersive materials. Extension of the approach to electromagnetic scenarios where the magnetic permeability is also dispersive, or to general dispersive bianisotropic medium is left to future work.

A generalized dispersive material (GDM) model [11] is used to represent dielectric functions in frequency space using rational functions. These rational approximations can represent a general class of linear dispersive effects for optical materials. In the time domain the GDM model is represented as a collection of ordinary differential equations using the so-called auxiliary differential equation (ADE) approach. Different materials may have different number of ADEs to approximate the rich and diverse physics of light-matter interaction. Maxwell's equations are solved in second-order form for the electric field and these are coupled to the ADEs. The solution in the interior is advanced using the recently developed high-order accurate schemes described in [12]. These high-order accurate finite difference schemes are single-stage schemes that use only three solution levels in time and have the same order of accuracy in space and time. Using only three time-levels is useful to avoid excessive storage requirements especially when there are many ADEs, corresponding to many terms in the rational representations in the GDM model.

Composite overlapping grids are used to accurately treat complex geometry with boundary conforming grids. Figure 1 shows some sample simulations using the new scheme on various geometrical configurations. Since most of the domain is usually covered by Cartesian grids, the schemes are very efficient. This paper extends the schemes from [12] to treat interfaces between different dispersive and/or non-dispersive materials. The interface is represented with conforming grids which enables high-order accuracy to be achieved even in the presence of jumps in material parameters and dispersive models. High-order accurate interface approximations are developed that retain the compact three-level approach. A novel hierarchical approach is developed to solve the interface equations that avoids the need to solve a large coupled set of equations along the interface.

The interface approximations are based on compatibility conditions derived from the interface jump conditions and the governing equations. For example, time-derivatives of the fundamental

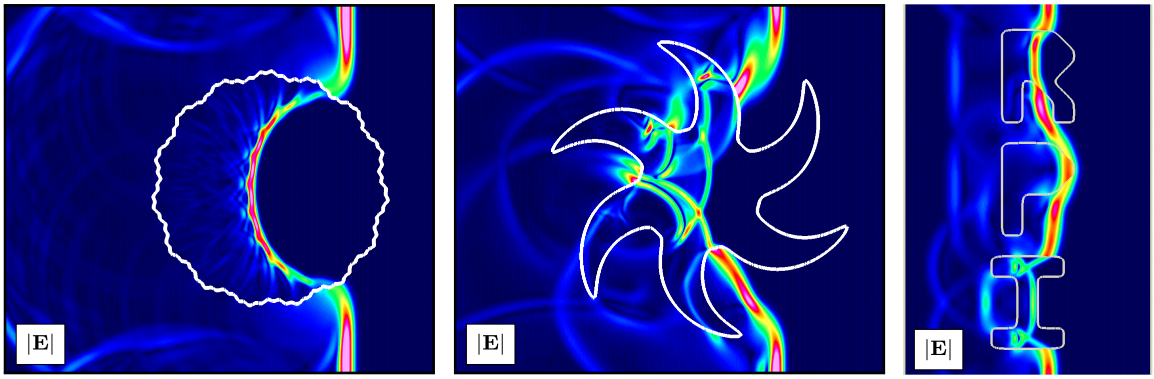

Figure 1: Scattering of a Gaussian plane wave from various material objects computed using the high-order time-stepping scheme with new high-order accurate interface approximations. These representative solutions illustrate the ability of the approach to treat complex interfaces.

interface conditions can be transformed using the governing equations into jump conditions on higher space derivatives of the solutions. These conditions provide *centered* approximations to determine the ghost point values adjacent to each side of the interface. The use of compatibility conditions tends to be more stable and accurate than using one-sided approximations. In addition, there is no reduction in the stable CFL-one time-step due to the boundary or interface treatement (one-sided approximations may reduce the stable time-step).

An important new development presented in this article concerns the solution to the discrete interface equations that result from application of the compatibility conditions. The new approach we describe here decouples the interface equations in the tangential direction; this is important for efficiency to avoid the solution of a coupled set of equations along the interface. This new decoupling approach will be useful more generally for other applications when compatbility conditions are used to discretrize interfaces or boundary conditions.

The stability of the interface approximations is examined using mode analysis. For example, it is shown with a model problem analysis, that the numerical scheme for a coupled problem with two materials remains stable provided the scheme for each materials in isolation is stable. Numerical results are presented in two and three space dimensions to confirm the accuracy and stability of the schemes. Exact solutions are derived for scattering from a disk in two dimensions and sphere in three dimensions when the materials inside and outside the bodies are modeled using GDM models.

The literature on time-domain schemes for Maxwell's equations is extensive. The Yee FDTD scheme [13] and its variants are among some of the most widely used in practice. There are also many other methods available based on finite difference, spectral, pseudo-spectral, finite-element, and discontinuous Galerkin methods, among others. The literature is very broad, and good overviews can be found in the review by Hestaven [14], or the references books by Taflove [15] and Cohen [16]. Typically, interfaces between materials are treated with an *embedded boundary* (EB) type approach or a *conforming boundary* (CB) approach. In its simplest form, the EB approach is straightforward to implement and uses a stair-step approximation to the interface with material properties changing discontinuously in cells adjacent to the interface; this results in a large local error in the solution (since certain solution components are discontinuous) but that on average may be between first and second-order accurate away from the interface. With extra effort, embedded boundary approximations can be made high-order accurate (see for example [17]), but it may be difficult to maintain the stability of the scheme. The CB approach requires conforming grids which may use unstructured or structured grids but this generally requires more effort to generate the grid compared to the EB approach. The CB approach can maintain multi-valued solutions on the interface and this makes it easier to design high-order accurate approximations.

The remainder of the article is organized as follows. In Section 2 the governing equations for the ADE-GDM model are presented together with the appropriate interface conditions. Section 3 introduces the time-stepping schemes and their discretization on overset grids. The numerical interface conditions are derived and discretized in Section 4. The stability of the numerical schemes is considered in Section 5. Numerical results are presented in Section 6 while conclusions are given in Section 7.

2. Governing Equations

We consider the solution to the time-domain Maxwell's equations in a domain Ω in n_d space dimensions consisting of N material sub-domains Ω_k,

$$\Omega = \bigcup_{k=1}^{N} \Omega_k,$$

see Figure 2. Each sub-domain is assumed to be a linear dispersive material, in general, so that Maxwell's equations in first-order form are given by

$$\partial_t \mathbf{D} = \nabla \times \mathbf{H}, \qquad \mathbf{x} \in \Omega_k, \tag{1a}$$

$$\mu_0 \partial_t \mathbf{H} = -\nabla \times \mathbf{E}, \qquad \mathbf{x} \in \Omega_k, \tag{1b}$$

$$\nabla \cdot \mathbf{D} = 0, \quad \nabla \cdot \mathbf{H} = 0, \qquad \mathbf{x} \in \Omega_k, \tag{1c}$$

$$\mathbf{D} = \epsilon_0 \mathbf{E} + \mathbf{P}, \tag{1d}$$

where $\mathbf{D} = \mathbf{D}(\mathbf{x}, t)$ is the displacement vector, $\mathbf{E} = \mathbf{E}(\mathbf{x}, t)$ is the electric field, $\mathbf{H} = \mathbf{H}(\mathbf{x}, t)$ is the magnetic field, $\mathbf{P} = \mathbf{P}(\mathbf{x}, t)$ is the (total) electric polarization vector, and ϵ_0 and μ_0 are, respectively, the vacuum permittivity and permeability. We have assumed negligible magnetic polarization so that $\mathbf{B} = \mu_0 \mathbf{H}$, where $\mathbf{B}$ is the magnetic flux density. For dispersive materials, $\mathbf{D}$ is assumed to be related to $\mathbf{E}$ through a convolution,

$$\mathbf{D}(\mathbf{x}, t) = \epsilon(t) * \mathbf{E}(\mathbf{x}, t) = \int_{-\infty}^{\infty} \epsilon(\tau)\, \mathbf{E}(\mathbf{x}, t - \tau)\, d\tau,$$

where $\epsilon(t)$ is the electric permittivity (assumed spatially constant in each sub-domain Ω_d). The Fourier transform in time of a variable is denoted with a "hat" and we use the convention

$$\hat{\mathbf{D}}(\mathbf{x}, \omega) = \int_{-\infty}^{\infty} e^{i\omega t}\, \mathbf{D}(\mathbf{x}, t)\, dt, \qquad \mathbf{D}(\mathbf{x}, t) = \frac{1}{2\pi} \int_{-\infty}^{\infty} e^{-i\omega t}\, \hat{\mathbf{D}}(\mathbf{x}, \omega)\, d\omega.$$

In the frequency domain, $\hat{\mathbf{D}}$ and $\hat{\mathbf{E}}$ are related by

$$\hat{\mathbf{D}} = \hat{\epsilon}\, \hat{\mathbf{E}} = \epsilon_0\, \hat{\mathbf{E}} + \hat{\mathbf{P}} = \epsilon_0 \big(1 + \chi(-i\omega)\big) \hat{\mathbf{E}},$$

$$\hat{\mathbf{P}} = \epsilon_0 \chi(-i\omega)\, \hat{\mathbf{E}},$$

where $\hat{\epsilon}$ is the electric permittivity in the frequency domain and χ is the electric susceptibility. Dispersive effects are modeled with a generalized dispersive material (GDM) model [11]. The GDM model takes the form of a rational approximation to the electric susceptibility,

$$\chi(s) \overset{\text{def}}{=} \sum_{m=1}^{N_p} \frac{a_{0,m} + s\, a_{1,m}}{b_{0,m} + s\, b_{1,m} + s^2}, \tag{2}$$

where the coefficients $(a_{0,m}, a_{1,m}, b_{0,m}, b_{1,m})$ are taken to be spatially constant over each separate material domain Ω_k. (This spatial dependence of the GDM coefficients has been suppressed here for notational convenience.)

Following [12], we consider the system in (1) in second-order form and use an auxiliary differential equation (ADE) approach to describe the evolution of the polarization vector. These equations have the form

$$\partial_t^2 \mathbf{E} = c^2 \Delta \mathbf{E} - \epsilon_0^{-1} \partial_t^2 \mathbf{P}, \qquad \mathbf{x} \in \Omega_k \tag{3a}$$

$$\partial_t^2 \mathbf{P}_m + b_{1,m} \partial_t \mathbf{P}_m + b_{0,m} \mathbf{P}_m = \epsilon_0 \big[a_{0,m} \mathbf{E} + a_{1,m} \partial_t \mathbf{E} \big], \qquad \mathbf{x} \in \Omega_k, \quad m = 1, 2, \ldots, N_p, \tag{3b}$$

$$\mathbf{P} \overset{\text{def}}{=} \sum_{m=1}^{N_p} \mathbf{P}_m. \tag{3c}$$

where $c^2 = 1/(\epsilon_0 \mu_0)$ is the nominal wave speed. The total polarization vector is governed by a generalized dispersive material (GDM) model, which consists of a sum of N_p component polarization vectors $\mathbf{P}_m$, each satisfying a second-order ordinary differential equation with coefficients from (2). The number of component vectors and the coefficients are chosen to fit a given dispersion model or spectroscopic data (see [12] for further details). We note that the material in Ω_k may be non-dispersive in which case $\mathbf{P} = 0$ for that sub-domain.

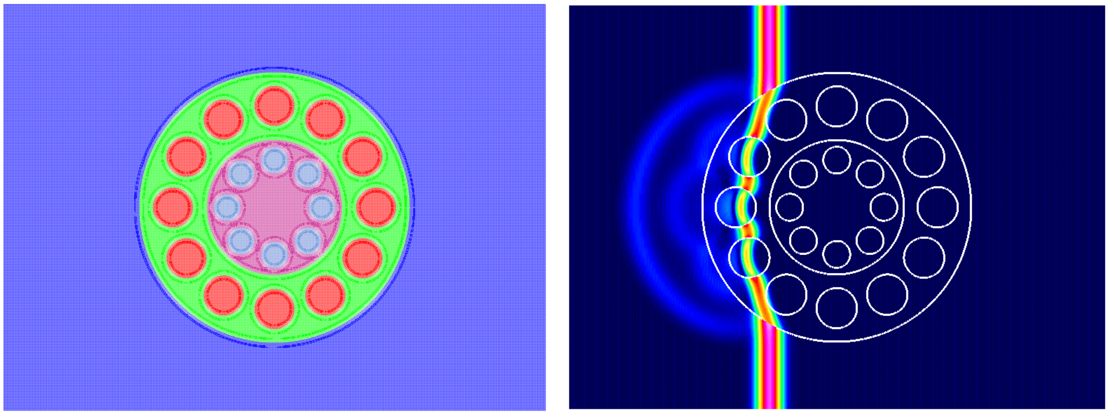

Figure 2: Left: A composite grid used for a multi-material scattering problem showing different material domains Ω_d. Right: contours of $|\mathbf{E}|$ for scattering of a Gaussian traveling wave; see Section 6.4 for more details.

The second-order system in (3) requires appropriate initial conditions, boundary conditions and interface conditions. Initial conditions for $\mathbf{E}$ and $\mathbf{P}_m$ are

$$\mathbf{E}(\mathbf{x}, 0) = \mathbf{E}^0(\mathbf{x}), \qquad \partial_t \mathbf{E}(\mathbf{x}, 0) = \mathbf{E}^1(\mathbf{x}), \qquad \mathbf{x} \in \Omega_k \tag{4a}$$

$$\mathbf{P}_m(\mathbf{x},0) = \mathbf{P}_m^0(\mathbf{x}), \qquad \partial_t \mathbf{P}_m(\mathbf{x},0) = \mathbf{P}_m^1(\mathbf{x}), \quad \mathbf{x} \in \Omega_k \quad m = 1,2,\ldots,N_p, \tag{4b}$$

where $\mathbf{E}^0(\mathbf{x})$, $\mathbf{E}^1(\mathbf{x})$, $\mathbf{P}_m^0(\mathbf{x})$ and $\mathbf{P}_m^1(\mathbf{x})$ are given functions. Let Γ_k denote the boundary of Ω_k. A portion of Ω_k may be a physical boundary, such as a PEC boundary, or an interface with another sub-domain. At a PEC boundary, for example, the tangential components of $\mathbf{E}$ are zero, which can be expressed as

$$\mathbf{n} \times \mathbf{E} = \mathbf{0}, \qquad \mathbf{x} \in \partial\Gamma_{\text{PEC}}, \tag{5}$$

where $\mathbf{n}$ is a unit normal to Γ_{PEC}. The second-order form of Maxwell's equations in (3a) requires another boundary condition for $\mathbf{E}$, and the appropriate condition is to specify the divergence of the field to be zero

$$\nabla \cdot \mathbf{E} = 0, \qquad \mathbf{x} \in \partial\Gamma_{\text{PEC}}. \tag{6}$$

Note that no boundary conditions are needed for $\mathbf{P}_m$ since its evolution is determined by the ODE in (3b).

At an interface, Γ, between materials Ω_{k_1} and Ω_{k_2} (dispersive or not), the primary jump conditions for the first-order system in (1) are

$$\left[\mathbf{n} \times \mathbf{E}\right]_I = 0, \qquad \mathbf{x} \in \Gamma, \tag{7a}$$
$$\left[\mathbf{n} \cdot \mathbf{D}\right]_I = 0, \qquad \mathbf{x} \in \Gamma, \tag{7b}$$
$$\left[\mathbf{n} \times \mathbf{H}\right]_I = 0, \qquad \mathbf{x} \in \Gamma, \tag{7c}$$
$$\left[\mu_0\, \mathbf{n} \cdot \mathbf{H}\right]_I = 0, \qquad \mathbf{x} \in \Gamma, \tag{7d}$$

where $[\cdot]_I$ denotes the jump across the interface [18]. For the second-order form of the dispersive Maxwell's equations in (3), the primary jump conditions become

$$\left[\mathbf{n} \times \mathbf{E}\right]_I = 0, \qquad \mathbf{x} \in \Gamma, \tag{8a}$$
$$\left[\mathbf{n} \cdot (\epsilon_0 \mathbf{E} + \mathbf{P})\right]_I = 0, \qquad \mathbf{x} \in \Gamma, \tag{8b}$$
$$\left[\mu_0^{-1}\, \mathbf{n} \times \nabla \times \mathbf{E}\right]_I = 0, \qquad \mathbf{x} \in \Gamma, \tag{8c}$$
$$\left[\nabla \cdot \mathbf{E}\right]_I = 0, \qquad \mathbf{x} \in \Gamma. \tag{8d}$$

The condition in (8b) follows from the definition of $\mathbf{D}$ in (1d), while (8c) follows by taking the time derivative of (7c). The final condition in (8d) is taken to ensure that $\nabla \cdot \mathbf{D} = \nabla \cdot \mathbf{E} = \nabla \cdot \mathbf{P} = 0$.

3. Time-stepping schemes on overlapping grids

A principal aim of this article is to describe second and fourth-order accurate implementations of the jump conditions in (8) that can be used in the time-stepping schemes for the dispersive Maxwell's equations discussed previously in [12]. To this end, we summarize briefly the second and fourth-order accurate time-stepping schemes in Section 3.1 and the discretization on overlapping grids in Section 3.2. Further details can be found in [12].

3.1. Second and fourth-order accurate time-stepping schemes

Let $\mathbf{x}_{\mathbf{j}} \in \mathbb{R}^n_d$ denote the grid points on a structured grid, where $\mathbf{j} = (j_1, \dots, j_d) \in \mathbb{Z}^n_d$ is a multi-index of integers. Let $\mathbf{E}^n_{\mathbf{j}}$ and $\mathbf{P}^n_{m,\mathbf{j}}$ denote grid functions that approximate $\mathbf{E}(\mathbf{x}_{\mathbf{j}}, t^n)$ and $\mathbf{P}_m(\mathbf{x}_{\mathbf{j}}, t^n)$, respectively, at time level $t^n = n\Delta t$. A second-order accurate approximation to (3a)–(3b) is given by

$$D_{+t}D_{-t}\mathbf{E}^n_{\mathbf{j}} = c^2\Delta_{2h}\mathbf{E}^n_{\mathbf{j}} - \epsilon_0^{-1}D_{+t}D_{-t}\mathbf{P}^n_{\mathbf{j}}, \tag{9a}$$

$$D_{+t}D_{-t}\mathbf{P}^n_{m,\mathbf{j}} + b_{1,m}D_{0t}\mathbf{P}^n_{m,\mathbf{j}} + b_{0,m}\mathbf{P}^n_{m,\mathbf{j}} = \tilde{a}_{0,m}\mathbf{E}^n_{\mathbf{j}} + \tilde{a}_{1,m}D_{0t}\mathbf{E}^n_{\mathbf{j}}, \quad m = 1, 2, \dots, N_p \tag{9b}$$

where

$$\mathbf{P}^n_{\mathbf{j}} \overset{\text{def}}{=} \sum_{m=1}^{N_p} \mathbf{P}^n_{m,\mathbf{j}}, \tag{10}$$

and

$$\tilde{a}_{0,m} \overset{\text{def}}{=} \epsilon_0\, a_{0,m}, \qquad \tilde{a}_{1,m} \overset{\text{def}}{=} \epsilon_0\, a_{1,m}, \qquad m = 1, 2, \dots, N_p,$$

are scaled GDM parameters. Here, Δ_{2h} denotes a second-order accurate approximation to the Laplace operator, while D_{+t}, D_{-t}, and D_{0t} denote the usual forward, backward, and central divided difference approximations of the first-derivative operator with respect to time, defined by

$$D_{+t}\mathbf{W}^n_{\mathbf{j}} \overset{\text{def}}{=} \frac{\mathbf{W}^{n+1}_{\mathbf{j}} - \mathbf{W}^n_{\mathbf{j}}}{\Delta t}, \qquad D_{-t}\mathbf{W}^n_{\mathbf{j}} \overset{\text{def}}{=} \frac{\mathbf{W}^n_{\mathbf{j}} - \mathbf{W}^{n-1}_{\mathbf{j}}}{\Delta t}, \qquad D_{0t}\mathbf{W}^n_{\mathbf{j}} \overset{\text{def}}{=} \frac{\mathbf{W}^{n+1}_{\mathbf{j}} - \mathbf{W}^{n-1}_{\mathbf{j}}}{2\Delta t},$$

for some generic grid function $\mathbf{W}^n_{\mathbf{j}}$. Thus, $D_{+t}D_{-t}$ is a centered approximation of the second-derivative operator with respect to time. The approximation in (9) is a compact, three-level time-stepping scheme, which leads to explicit formulas for $\mathbf{E}^{n+1}_{\mathbf{j}}$ and $\mathbf{P}^{n+1}_{m,\mathbf{j}}$.

Algorithm 1 Second-order accurate ADE-GDM algorithm.

```
$t = 0, n = 0$;
$\mathbf{E}^0_{\mathbf{j}} = \mathbf{E}^0(\mathbf{x}_{\mathbf{j}}),\quad \mathbf{E}^1_{\mathbf{j}} = \mathbf{E}^0(\mathbf{x}_{\mathbf{j}}) + \Delta t\mathbf{E}^1(\mathbf{x}_{\mathbf{j}}) + \frac{\Delta t^2}{2}\partial_t^2\mathbf{E}(\mathbf{x}_j, 0)$;    ▷ Initialize $\mathbf{E}^0_{\mathbf{j}},\ \mathbf{E}^1_{\mathbf{j}}$
for $m = 1, \dots, N_p$ do
    $\mathbf{P}^0_{m,\mathbf{j}} = \mathbf{P}^0_m(\mathbf{x}_{\mathbf{j}}),\quad \mathbf{P}^1_{m,\mathbf{j}} = \mathbf{P}^0_m(\mathbf{x}_{\mathbf{j}}) + \mathbf{P}^1_m(\mathbf{x}_{\mathbf{j}})\Delta t + \frac{\Delta t^2}{2}\partial_t^2\mathbf{P}_m(\mathbf{x}_j, 0)$;    ▷ Inititialize $\mathbf{P}^0_{m,\mathbf{j}},\ \mathbf{P}^1_{m,\mathbf{j}}$
    $\beta_m = (1 + \frac{\Delta t}{2}\, b_{1,m})^{-1}$;
end for
$\beta = \frac{\Delta t}{2} \sum_m \tilde{a}_{1,m}\, \beta_m$;
while $t < t_{\text{final}}$ do    ▷ Begin time-stepping loop
    for $m = 1, \dots, N_p$ do
        $\mathbf{R}_m = 2\mathbf{P}^n_{m,\mathbf{j}} - \mathbf{P}^{n-1}_{m,\mathbf{j}} + \frac{\Delta t}{2}\, b_{1,m}\mathbf{P}^{n-1}_{m,\mathbf{j}} - \Delta t^2\, b_{0,m}\mathbf{P}^n_{m,\mathbf{j}} + \Delta t^2\, \tilde{a}_{0,m}\mathbf{E}^n_{\mathbf{j}} - \frac{\Delta t}{2}\, \tilde{a}_{1,m}\mathbf{E}^{n-1}_{\mathbf{j}}$;
    end for
    $\mathbf{R} = \sum_m \beta_m\mathbf{R}_m$;
    $\mathbf{E}^{n+1}_{\mathbf{j}} = (1 + \epsilon_0^{-1}\beta)^{-1}\Big[2\mathbf{E}^n_{\mathbf{j}} - \mathbf{E}^{n-1}_{\mathbf{j}} + \Delta t^2 c^2\Delta_{2h}\mathbf{E}^n_{\mathbf{j}} + \epsilon_0^{-1}\sum_m \Big\{2\mathbf{P}^n_{m,\mathbf{j}} - \mathbf{P}^{n-1}_{m,\mathbf{j}}\Big\} - \epsilon_0^{-1}\,\mathbf{R}\Big]$;
    for $m = 1, \dots, N_p$ do
        $\mathbf{P}^{n+1}_{m,\mathbf{j}} = \frac{\Delta t}{2}\, \tilde{a}_{1,m}\, \beta_m\, \mathbf{E}^{n+1}_{\mathbf{j}} + \beta_m\, \mathbf{R}_m$;
    end for
    $t = t + \Delta t,\ n = n + 1$;
    Apply boundary and interface conditions.
end while    ▷ End time-stepping loop
```

The implementation of the second-order accurate time-stepping scheme is given in Algorithm 1. The grid functions, $\mathbf{E}_{\mathbf{j}}^0$ and $\mathbf{P}_{m,\mathbf{j}}^0$, at time level $t^0 = 0$ are determined from the initial conditions, while the grid functions at the first time step, $t^1 = \Delta t$, are evaluated using a Taylor series in time. (Note that some typographic errors appeared in the original second and fourth-order accurate algorithms given in [12]. These errors are corrected in Algorithms 1 and 2 given here.) In the time-stepping loop (lines 8–19), the second-order accurate explicit updates for $\mathbf{E}_{\mathbf{j}}^{n+1}$ and $\mathbf{P}_{m,\mathbf{j}}^{n+1}$ are determined in lines 13 and 15, respectively. To obtain the formulas for these updates, we note that (9b) can be solved for $\mathbf{P}_{m,\mathbf{j}}^{n+1}$ in terms of $\mathbf{E}_{\mathbf{j}}^{n+1}$ and a remainder,

$$\mathbf{P}_{m,\mathbf{j}}^{n+1} = \frac{\Delta t}{2}\, \tilde{a}_{1,m}\, \beta_m\, \mathbf{E}_{\mathbf{j}}^{n+1} + \beta_m\, \mathbf{R}_m, \tag{11}$$

where β_m and $\mathbf{R}_m$ are defined on lines 5 and 10, respectively. Equation (11) can be summed over m to determine $\mathbf{P}_{\mathbf{j}}^{n+1}$ in terms of $\mathbf{E}_{\mathbf{j}}^{n+1}$ and another remainder. This equation for $\mathbf{P}_{\mathbf{j}}^{n+1}$ is substituted into (9a) and subsequently solved for $\mathbf{E}_{\mathbf{j}}^{n+1}$. Given $\mathbf{E}_{\mathbf{j}}^{n+1}$, the values of $\mathbf{P}_{m,\mathbf{j}}^{n+1}$ are found from (11).

An important step in Algorithm 1 occurs at line 18, marked in blue, where the boundary and interface conditions are applied. A detailed discussion of this step of the algorithm for an interface separating two materials is new and given in Section 4.1.

A fourth-order accurate time-stepping scheme can be constructed using a modified equation approach starting with the second-order accurate scheme in (9). A key step involves Taylor series expansions of the form

$$D_{+t}D_{-t}\mathbf{W}(\mathbf{x},t) = \partial_t^2\mathbf{W} + \frac{2\Delta t^2}{4!}\partial_t^4\mathbf{W} + \mathcal{O}(\Delta t^4), \tag{12}$$

where $\mathbf{W}$ represents either $\mathbf{E}$ or $\mathbf{P}$. The governing equations in (3), and their time derivatives, are then used to express (12) in the form of a three-level time-stepping scheme. The resulting fourth-order accurate scheme is

$$\begin{aligned}
D_{+t}D_{-t}\mathbf{E}_{\mathbf{j}}^n &= c^2\Delta_{4h}\mathbf{E}_{\mathbf{j}}^n - \epsilon_0^{-1}D_{+t}D_{-t}\mathbf{P}_{\mathbf{j}}^n \\
&\qquad + \frac{\Delta t^2}{12}\Big((c^2\Delta_{2h})^2\mathbf{E}_{\mathbf{j}}^n - \epsilon_0^{-1}c^2\,\Delta_{2h}\partial_t^2\mathbf{P}^*\big|_{\mathbf{j}}^n\Big),
\end{aligned} \tag{13a}$$

$$\begin{aligned}
D_{+t}D_{-t}\mathbf{P}_{m,\mathbf{j}}^n &= -b_{1,m}\Big(D_{0t}\mathbf{P}_{m,\mathbf{j}}^n - \frac{\Delta t^2}{6}\,\partial_t^3\mathbf{P}_m^*\big|_{\mathbf{j}}^n\Big) - b_{0,m}\mathbf{P}_{m,\mathbf{j}}^n \\
&\qquad + \tilde{a}_{0,m}\mathbf{E}_{\mathbf{j}}^n + \tilde{a}_{1,m}\Big(D_{0t}\mathbf{E}_{\mathbf{j}}^n - \frac{\Delta t^2}{6}\,\partial_t^3\mathbf{E}^*\big|_{\mathbf{j}}^n\Big) \\
&\qquad\quad + \frac{\Delta t^2}{12}\Big(-b_{1,m}\,\partial_t^3\mathbf{P}_m^*\big|_{\mathbf{j}}^n - b_{0,m}D_{+t}D_{-t}\mathbf{P}_{m,\mathbf{j}}^n \\
&\qquad\qquad + \tilde{a}_{0,m}D_{+t}D_{-t}\mathbf{E}_{\mathbf{j}}^n + \tilde{a}_{1,m}\,\partial_t^3\mathbf{E}^*\big|_{\mathbf{j}}^n\Big),
\end{aligned} \tag{13b}$$

where Δ_{4h} is a fourth-order accurate approximation of the Laplacian operator, $\mathbf{P}_{\mathbf{j}}^n$ is given in (10), and $\partial_t^3\mathbf{E}^*\big|_{\mathbf{j}}^n$, $\partial_t^3\mathbf{P}_m^*\big|_{\mathbf{j}}^n$ and $\Delta_{2h}\partial_t^2\mathbf{P}^*\big|_{\mathbf{j}}^n$ are second-order accurate approximations. Note that the terms highlighted in blue (here and elsewhere) indicate second-order accurate approxmations and the asterisk is used to denote terms in (13) that are computed using the second-order accurate time-stepping scheme.

Algorithm 2 describes the implementation of the fourth-order accurate time-stepping scheme.

Algorithm 2 Fourth-order accurate ADE-GDM algorithm.

```
$t = 0, n = 0;$
$\mathbf{E}^0_{\mathbf{j}} = \mathbf{E}^0(\mathbf{x}_{\mathbf{j}});$    ▷ Initialize $\mathbf{E}^0_{\mathbf{j}},\ \mathbf{E}^1_{\mathbf{j}}$
$\mathbf{E}^1_{\mathbf{j}} = \mathbf{E}^0(\mathbf{x}_{\mathbf{j}}) + \Delta t \mathbf{E}^1(\mathbf{x}_{\mathbf{j}}) + \frac{\Delta t^2}{2} \partial_t^2 \mathbf{E}(\mathbf{x}_{\mathbf{j}}, 0) + \frac{\Delta t^3}{3!} \partial_t^3 \mathbf{E}(\mathbf{x}_{\mathbf{j}}, 0) + \frac{\Delta t^4}{4!} \partial_t^4 \mathbf{E}(\mathbf{x}_{\mathbf{j}}, 0);$
for $m = 1, \ldots, N_p$ do
    $\mathbf{P}^0_{m,\mathbf{j}} = \mathbf{P}^0_m(\mathbf{x}_{\mathbf{j}});$    ▷ Inititialize $\mathbf{P}^0_{m,\mathbf{j}},\ \mathbf{P}^1_{m,\mathbf{j}}$
    $\mathbf{P}^1_{m,\mathbf{j}} = \mathbf{P}^0_m(\mathbf{x}_{\mathbf{j}}) + \Delta t \mathbf{P}^1_m(\mathbf{x}_{\mathbf{j}}) + \frac{\Delta t^2}{2} \partial_t^2 \mathbf{P}_m(\mathbf{x}_{\mathbf{j}}, 0) + \frac{\Delta t^3}{3!} \partial_t^3 \mathbf{P}_m(\mathbf{x}_{\mathbf{j}}, 0) + \frac{\Delta t^4}{4!} \partial_t^4 \mathbf{P}_m(\mathbf{x}_{\mathbf{j}}, 0);$
    $\beta_m = (1 + \frac{\Delta t}{2} b_{1,m})^{-1};$
end for
$\beta = (\Delta t/2) \sum_m \tilde{a}_{1,m} \beta_m;$
while $t < t_{final}$ do
    for $m = 1, \ldots, N_p$ do    ▷ Evaluate second-order accurate predictions $\mathbf{E}^{*\,n+1}_{\mathbf{j}}, \mathbf{P}^{*\,n+1}_{m,\mathbf{j}}$
        $\mathbf{R}_m = 2\mathbf{P}^n_{m,\mathbf{j}} - \mathbf{P}^{n-1}_{m,\mathbf{j}} + \frac{\Delta t}{2} b_{1,m} \mathbf{P}^{n-1}_{m,\mathbf{j}} - \Delta t^2 b_{0,m} \mathbf{P}^n_{m,\mathbf{j}} + \Delta t^2 \tilde{a}_{0,m} \mathbf{E}^n_{\mathbf{j}} - \frac{\Delta t}{2} \tilde{a}_{1,m} \mathbf{E}^{n-1}_{\mathbf{j}};$
    end for
    $\mathbf{R} = \sum_m \beta_m \mathbf{R}_m;$
    $\mathbf{E}^{*\,n+1}_{\mathbf{j}} = (1 + \epsilon_0^{-1} \beta)^{-1} \Big[ 2\mathbf{E}^n_{\mathbf{j}} - \mathbf{E}^{n-1}_{\mathbf{j}} + \Delta t^2 c^2 \Delta_{2h} \mathbf{E}^n_{\mathbf{j}} + \epsilon_0^{-1} \sum_m \Big\{ 2\mathbf{P}^n_{m,\mathbf{j}} - \mathbf{P}^{n-1}_{m,\mathbf{j}} \Big\} - \epsilon_0^{-1} \mathbf{R} \Big];$
    $\partial_t \mathbf{E}^*\big|^n_{\mathbf{j}} = (\mathbf{E}^{*\,n+1}_{\mathbf{j}} - \mathbf{E}^{n-1}_{\mathbf{j}})/(2\Delta t);$    $\partial_t^2 \mathbf{E}^*\big|^n_{\mathbf{j}} = (\mathbf{E}^{*\,n+1}_{\mathbf{j}} - 2\mathbf{E}^n_{\mathbf{j}} + \mathbf{E}^{n-1}_{\mathbf{j}})/\Delta t^2;$
    $\Delta_{2h} \partial_t \mathbf{E}^*\big|^n_{\mathbf{j}} = \Delta_{2h} (\mathbf{E}^{*\,n+1}_{\mathbf{j}} - \mathbf{E}^{n-1}_{\mathbf{j}})/(2\Delta t);$
    for $m = 1, \ldots, N_p$ do
        $\mathbf{P}^{*\,n+1}_{m,\mathbf{j}} = \frac{\Delta t}{2} \tilde{a}_{1,m} \beta_m \mathbf{E}^{*\,n+1}_{\mathbf{j}} + \beta_m \mathbf{R}_m;$
        $\partial_t \mathbf{P}^*_m\big|^n_{\mathbf{j}} = (\mathbf{P}^{*\,n+1}_{m,\mathbf{j}} - \mathbf{P}^{n-1}_{m,\mathbf{j}})/(2\Delta t);$
        $\partial_t^3 \mathbf{P}^*_m\big|^n_{\mathbf{j}} = b^{(3)}_{1,m} \partial_t \mathbf{P}^*_m\big|^n_{\mathbf{j}} + b^{(3)}_{0,m} \mathbf{P}_{m,\mathbf{j}} + \tilde{a}^{(3)}_{0,m} \mathbf{E}_{\mathbf{j}} + \tilde{a}^{(3)}_{1,m} \partial_t \mathbf{E}^*\big|^n_{\mathbf{j}} + \tilde{a}^{(3)}_{2,m} \partial_t^2 \mathbf{E}^*\big|^n_{\mathbf{j}};$
    end for
    $\mathbf{P}^{*\,n+1}_{\mathbf{j}} = \sum_m \mathbf{P}^{*\,n+1}_{m,\mathbf{j}};$
    $\Delta_{2h} \partial_t^2 \mathbf{P}^*\big|^n_{\mathbf{j}} = \Delta_{2h} (\mathbf{P}^{*\,n+1}_{\mathbf{j}} - 2\mathbf{P}^n_{\mathbf{j}} + \mathbf{P}^{n-1}_{\mathbf{j}})/\Delta t^2;$    $\partial_t^3 \mathbf{E}^*\big|^n_{\mathbf{j}} = c^2 \Delta_{2h} \partial_t \mathbf{E}^*\big|^n_{\mathbf{j}} - \epsilon_0^{-1} \partial_t^3 \mathbf{P}^*\big|^n_{\mathbf{j}};$
    for $m = 1, \ldots, N_p$ do    ▷ Evaluate fourth-order accurate updates $\mathbf{E}^{n+1}_{\mathbf{j}}, \mathbf{P}^{n+1}_{m,\mathbf{j}}$
        $\gamma_m = 1 + b_{1,m} \frac{\Delta t}{2} + b_{0,m} \frac{\Delta t^2}{12};$
        $\mathbf{R}_m = \left(1 + b_{1,m} \frac{\Delta t^2}{12}\right) \left(2\mathbf{P}^n_{m,\mathbf{j}} - \mathbf{P}^{n-1}_{m,\mathbf{j}}\right) + \frac{\Delta t}{2} b_{1,m} \mathbf{P}^{n-1}_{m,\mathbf{j}} - \Delta t^2 b_{0,m} \mathbf{P}^n_{m,\mathbf{j}} + \Delta t^2 \tilde{a}_{0,m} \mathbf{E}^n_{\mathbf{j}}$
                $- \frac{\Delta t}{2} \tilde{a}_{1,m} \mathbf{E}^{n-1}_{\mathbf{j}} - \tilde{a}_{0,m} \frac{\Delta t^2}{12} \left(2\mathbf{E}^n_{\mathbf{j}} - \mathbf{E}^{n-1}_{\mathbf{j}}\right) + b_{1,m} \frac{\Delta t^4}{12} \partial_t^3 \mathbf{P}^*_m\big|^n_{\mathbf{j}} - \tilde{a}_{1,m} \frac{\Delta t^4}{12} \partial_t^3 \mathbf{E}^*\big|^n_{\mathbf{j}};$
    end for
    $\gamma_E = \sum_m \frac{1}{\gamma_m} \left(-a_{1,m} \frac{\Delta t}{2} - a_{0,m} \frac{\Delta t^2}{12}\right);$    $\mathbf{R}_P = \sum_m \frac{1}{\gamma_m} \mathbf{R}_m;$
    $\mathbf{R}_E = 2\mathbf{E}^n_{\mathbf{j}} - \mathbf{E}^{n-1}_{\mathbf{j}} + (c\Delta t)^2 \Delta_{4h} \mathbf{E}^n_{\mathbf{j}} + \epsilon_0^{-1} \sum_m \Big\{ 2\mathbf{P}^n_{m,\mathbf{j}} - \mathbf{P}^{n-1}_{m,\mathbf{j}} \Big\} + \frac{\Delta t^4}{12} \Big( (c^2 \Delta_{2h})^2 \mathbf{E}^n_{\mathbf{j}} - \epsilon_0^{-1} c^2 \Delta_{2h} \partial_t^2 \mathbf{P}^*\big|^n_{\mathbf{j}} \Big)$
    $\mathbf{E}^{n+1}_{\mathbf{j}} = \left(\epsilon_0^{-1} \mathbf{R}_P - \mathbf{R}_E\right) / (\epsilon_0^{-1} \gamma_E - 1);$
    for $m = 1, \ldots, N_p$ do
        $\mathbf{P}^{n+1}_{m,\mathbf{j}} = \frac{1}{\gamma_m} \left[ \left(a_{1,m} \frac{\Delta t}{2} + a_{0,m} \frac{\Delta t^2}{12}\right) \mathbf{E}^{n+1}_{\mathbf{j}} + \mathbf{R}_m \right];$
    end for
    $t = t + \Delta t,\ n = n + 1;$
    Apply boundary and interface conditions.
end while
```

The numerical solution values at the first time step, $n = 1$ (lines 3 and 6), are determined using a Taylor series in time. The higher derivatives in these series are obtained using the governing equations evaluated at $t = 0$. For example, the second derivative of $\mathbf{P}_m$ at $t = 0$ can be obtained using (3b) and the initial conditions in (4) as

$$\partial_t^2 \mathbf{P}_m(\mathbf{x}_\mathbf{j}, 0) \overset{\text{def}}{=} \tilde{a}_{1,m}\mathbf{E}^1(\mathbf{x}_\mathbf{j}) + \tilde{a}_{0,m}\mathbf{E}^0(\mathbf{x}_\mathbf{j}) - b_{1,m}\mathbf{P}^1_m(\mathbf{x}_\mathbf{j}) - b_{0,m}\mathbf{P}^0_m(\mathbf{x}_\mathbf{j}).$$

In the time-stepping loop (lines 10–37), temporary second-order accurate updates are computed first in lines 11–24, which are then used to compute derived quantities, such as $\partial_t \mathbf{P}^*_m|^n_\mathbf{j}$ (line 20). The fourth-order accurate explicit updates for $\mathbf{E}^{n+1}_\mathbf{j}$ and $\mathbf{P}^{n+1}_{m,\mathbf{j}}$ are then performed in lines 31 and 33, respectively, using formulas obtained from (13a) and (13b) in an analogous fashion to the second-order updates. In particular, (13b) can be solved for $\mathbf{P}^{n+1}_{m,\mathbf{j}}$ in terms of $\mathbf{E}^{n+1}_\mathbf{j}$ and a remainder,

$$\mathbf{P}^{n+1}_{m,\mathbf{j}} = \frac{1}{\gamma_m}\left[\left(a_{1,m}\frac{\Delta t}{2} + a_{0,m}\frac{\Delta t^2}{12}\right)\mathbf{E}^{n+1}_\mathbf{j} + \mathbf{R}_m\right], \tag{14}$$

where γ_m and $\mathbf{R}_m$ are given in lines 26 and 27, respectively. Summing (14) for $m = 1, 2, \ldots, N_p$ leads to an equation for $\mathbf{P}^{n+1}_\mathbf{j}$ in terms of $\mathbf{E}^{n+1}_\mathbf{j}$, and then substituting this equation into (13a) and solving for $\mathbf{E}^{n+1}_\mathbf{j}$ leads to the update on line 31. Given $\mathbf{E}^{n+1}_\mathbf{j}$, the values for $\mathbf{P}^{n+1}_{m,\mathbf{j}}$ can then be evaluated from (14) which gives the update on line 33. As in the second-order scheme, an important step involves the application of interface conditions separating two materials, and this is new and discussed in detail in Section 4.2 for the fourth-order accurate scheme.

3.2. Discretization on overlapping grids

Each material sub-domain Ω_k in the computational domain is discretized with a composite overlapping grid (also known as an *overset grid*) as shown, for example, in Figures 2, 9, and 13. Composite grids allow the use of efficient finite-difference schemes on structured grids for complex geometry while maintaining high-order accuracy at curved boundaries and interfaces.

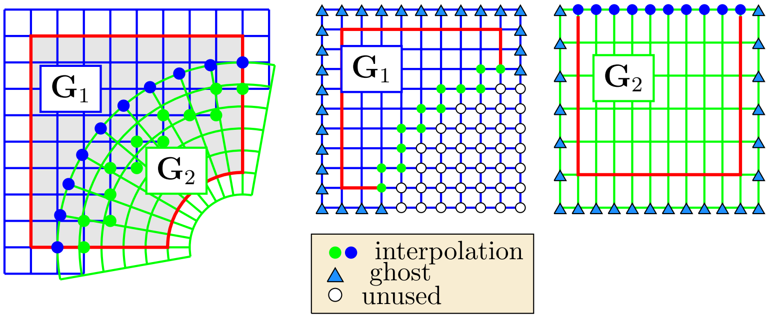

Figure 3: Left: an overlapping grid consisting of two structured curvilinear component grids, $\mathbf{x} = G_1(\mathbf{r})$ and $\mathbf{x} = G_2(\mathbf{r})$. Middle and right: component grids for the square and annular grids in the unit square parameter space $\mathbf{r}$. Grid points are classified as discretization points, interpolation points or unused points. Ghost points are used to apply boundary conditions.

A composite overlapping grid for the sub-domain Ω_k, denoted as $\mathcal{G}$, consists of a set of component grids $\mathcal{G}_g$, $g = 1, \ldots, \mathcal{N}_k$, that cover Ω_k. A simple composite grid in two dimensions is illustrated in

Figure 3. Each component grid, $\mathcal{G}_g$, is a logically rectangular, curvilinear grid defined by a smooth mapping from a unit square (or unit cube) parameter space $\mathbf{r}$ to physical space $\mathbf{x}$,

$$\mathbf{x} = \mathbf{G}_g(\mathbf{r}), \qquad \mathbf{r} \in [0,1]^{n_d}, \qquad \mathbf{x} \in \mathbb{R}^{n_d}. \tag{15}$$

Grid points are classified as discretization points (where the PDE or boundary/interface conditions are applied), interpolation points (where solutions are interpolated from other component grids) or unused points. Ghost points are use to implement boundary and interface conditions. The overlapping grid generator **Ogen** [19] from the *Overture* framework is used to construct the overlapping grid information. By a change of independent variables (i.e. $\mathbf{x}$ to $\mathbf{r}$), the governing equations are transformed to the unit square coordinates; this can be done in either conservative or non-conservative form [20]. The dependent variables (e.g. $\mathbf{E}$) remain in Cartesian coordinates. Solution values at interpolation points are evaluated using tensor-product Lagrange interpolation in the parameter space of the mapping $\mathbf{G}_g$. This is straightforward to accomplish given the unit square (or cube) coordinates of an interpolation point in the parameter space of the donor grid. For the second-order accurate scheme the interpolation uses a three-point stencil in each direction, while a five-point stencil is used for the fourth-order scheme as required to maintain accuracy [21]. A high-order upwind dissipation [12, 22] for wave equations in second-order form [23] is used to maintain stability on overlapping grids.

4. Numerical interface approximations

In this section, interface conditions are derived which can be used with the second and fourth-order accurate time-stepping schemes. These conditions are applied after the solution has been updated in the interior by the schemes described in Algorithms 1 and 2 for the second and fourth-order cases, respectively. It is thus assumed that the grid values in $\mathbf{E}_{\mathbf{j}}^n$ and $\mathbf{P}_{m,\mathbf{j}}^n$ are known in the interior and on the interface at the new time t^n, as well as being known at all points at the old time t^{n-1}. The goal is to assign values in the ghost points for the grid functions adjacent to the interface at time t^n; compact two-level (in time) update equations are derived to do this that make use of the solutions at times t^{n-1} and t^n. As the expressions in the update formulae can be quite complex, the precise definitions for some of the coefficients are omitted. The discussion instead focuses on a high-level description of the procedure that determines the coefficients with Maple scripts that generate the full expressions available as part of the CgMx software distribution[5].

4.1. Second-order accurate interface approximations

The primary interface conditions for the dispersive Maxwell's equations in second-order form are given in (8). Following [20], additional *compatibility* interface conditions can be derived from (8) by taking even derivatives with respect to time, and then using the governing equations in (3) to replace time derivatives by space derivatives. This is useful for specifying formulas that set ghost points. For example, taking two time derivatives of (8a) and using (3a) leads to the interface compatibility condition

$$\left[\mathbf{n} \times \partial_t^2 \mathbf{E}\right]_I = 0 \quad \Longrightarrow \quad \left[\mathbf{n} \times \left(c^2 \Delta \mathbf{E} - \epsilon_0^{-1} \partial_t^2 \mathbf{P}\right)\right]_I = 0, \qquad \mathbf{x} \in \Gamma. \tag{16a}$$

---

[5] CgMx is available from `overtureFramework.org`.

Likewise, taking two time derivatives of (8b) and using (3a) and (3b) gives

$$\left[\mathbf{n}\cdot(\epsilon_0\partial_t^2\mathbf{E}+\partial_t^2\mathbf{P})\right]_I=0 \quad\Longrightarrow\quad \left[\mu_0^{-1}\mathbf{n}\cdot\Delta\mathbf{E}\right]_I=0, \qquad \mathbf{x}\in\Gamma. \tag{16b}$$

The two compatability conditions in (16a) and (16b), along with the remaining two primary interface conditions in (8c) and (8d), form the set of interface conditions used in the second-order accurate scheme to determine the ghost values for $\mathbf{E}$ on either side of the interface. In particular, the conditions in (16a) and (8c) can be thought of as determining the tangential components of $\mathbf{E}$ in the ghost points, while the conditions in (16b) and (8d) can be regarded as determining the normal components.

The set of interface conditions are approximated to second-order accuracy in space to give

$$\left[\mathbf{n}\times\left(c^2\Delta_{2h}\mathbf{E}_{\mathbf{j}}^n-\epsilon_0^{-1}\,\partial_t^2\mathbf{P}\big|_{\mathbf{j}}^n\right)\right]_I=0, \qquad \mathbf{j}\in\Gamma_h, \tag{17a}$$

$$\left[\mu_0^{-1}\mathbf{n}\cdot\Delta_{2h}\mathbf{E}_{\mathbf{j}}^n\right]_I=0, \qquad \mathbf{j}\in\Gamma_h, \tag{17b}$$

$$\left[\mu_0^{-1}\mathbf{n}\times\nabla_{2h}\times\mathbf{E}_{\mathbf{j}}^n\right]_I=0, \qquad \mathbf{j}\in\Gamma_h, \tag{17c}$$

$$\left[\nabla_{2h}\cdot\mathbf{E}_{\mathbf{j}}^n\right]_I=0, \qquad \mathbf{j}\in\Gamma_h, \tag{17d}$$

where ∇_{2h} and Δ_{2h} denote second-order accurate approximations (with a three-point stencil in each coordinate direction) to the gradient and Laplace operators, respectively. The approximate set of interface conditions in (17) can be used to determine the ghost-point values for $\mathbf{E}_{\mathbf{j}}^n$ on both sides of the interface once a second-order accurate approximation to $\partial_t^2\mathbf{P}\big|_{\mathbf{j}}^n$ in (17a) is defined. (Note that here and elsewhere the blue highlighted terms indicate second-order accurate approximations of terms involving temporal derivatives of either $\mathbf{E}$ or $\mathbf{P}$.) One approach to approximating $\partial_t^2\mathbf{P}\big|_{\mathbf{j}}^n$ would be to use a second-order accurate backward difference formula

$$\partial_t^2\mathbf{P}\big|_{\mathbf{j}}^n\approx\frac{2\mathbf{P}_{\mathbf{j}}^n-5\mathbf{P}_{\mathbf{j}}^{n-1}+4\mathbf{P}_{\mathbf{j}}^{n-2}-\mathbf{P}_{\mathbf{j}}^{n-3}}{\Delta t^2}. \tag{18}$$

This approach could be used although it requires storage for an additional time-level, $\mathbf{P}_{\mathbf{j}}^{n-3}$, on the interface. In addition, the stability bound for the time-stepping scheme with this one-sided approximation would likely be worse than a corresponding scheme with a centered, compact approximation, thus leading to a smaller time step. Instead, our approach is to obtain an expression for $\partial_t^2\mathbf{P}\big|_{\mathbf{j}}^n$ involving a linear combination of $\Delta_{2h}\mathbf{E}_{\mathbf{j}}^n$ (which uses a centered, compact approximation) and the known values $\mathbf{E}_{\mathbf{j}}^n$, $\mathbf{E}_{\mathbf{j}}^{n-1}$, $\mathbf{P}_{m,\mathbf{j}}^n$ and $\mathbf{P}_{m,\mathbf{j}}^{n-1}$ on the interface. Such an expression has the form

$$\partial_t^2\mathbf{P}\big|_{\mathbf{j}}^n=K_0^{\partial_t^2\mathbf{P}}\Delta_{2h}\mathbf{E}_{\mathbf{j}}^n+c_0\,\mathbf{E}_{\mathbf{j}}^n+c_1\,\mathbf{E}_{\mathbf{j}}^{n-1}+\sum_{m=1}^{N_p}\left(d_{0,m}\,\mathbf{P}_{m,\mathbf{j}}^n+d_{1,m}\,\mathbf{P}_{m,\mathbf{j}}^{n-1}\right), \tag{19}$$

where $K_0^{\partial_t^2\mathbf{P}}$, $\{c_0,c_1\}$ and $\{d_{0,m},d_{1,m}\}$, $m=1,2,\ldots,N_p$, are constants. Note that the term $\Delta_{2h}\mathbf{E}_{\mathbf{j}}^n$ in (19), which involves the ghost points associated with the interface, modifies the coefficient of $\Delta_{2h}\mathbf{E}_{\mathbf{j}}^n$ in (17a), and thus the corresponding coefficients in the linear system that determines the values at the ghost points.

To derive an expression for $\partial_t^2\mathbf{P}\big|_{\mathbf{j}}^n$ in the form of (19), we start by considering the second-order accurate approximations of the governing equations in (9) with (10) for $\mathbf{j}$ on the interface, $\mathbf{j}\in\Gamma_h$.

Upon multiplication by Δt^2, these equations take the form

$$\mathbf{E}_{\mathbf{j}}^{n+1} + \frac{1}{\epsilon_0}\mathbf{P}_{\mathbf{j}}^{n+1} = (c\Delta t)^2 \Delta_{2h}\mathbf{E}_{\mathbf{j}}^{n} + \text{R.T.}, \qquad \mathbf{j} \in \Gamma_h, \tag{20a}$$

$$-\frac{\tilde{a}_{1,m}\Delta t}{2}\mathbf{E}_{\mathbf{j}}^{n+1} + \left(1 + \frac{b_{1,m}\Delta t}{2}\right)\mathbf{P}_{m,\mathbf{j}}^{n+1} = \text{R.T.}, \qquad \mathbf{j} \in \Gamma_h, \tag{20b}$$

where R.T. denotes a generic remainder term involving a linear combination of the known values $\mathbf{E}_{\mathbf{j}}^{n}$, $\mathbf{E}_{\mathbf{j}}^{n-1}$, $\mathbf{P}_{m,\mathbf{j}}^{n}$ and $\mathbf{P}_{m,\mathbf{j}}^{n-1}$ on the interface. Solving (20b) for $\mathbf{P}_{m,\mathbf{j}}^{n+1}$ and summing over m gives

$$\mathbf{P}_{\mathbf{j}}^{n+1} = \beta\mathbf{E}_{\mathbf{j}}^{n+1} + \text{R.T.}, \qquad \mathbf{j} \in \Gamma_h, \tag{21}$$

where β is defined in lines 5 and 7 of Algorithm 1. Eliminating $\mathbf{P}_{\mathbf{j}}^{n+1}$ from (20a) gives

$$\mathbf{E}_{\mathbf{j}}^{n+1} = \left(\frac{(c\Delta t)^2}{1+\beta\epsilon_0^{-1}}\right)\Delta_{2h}\mathbf{E}_{\mathbf{j}}^{n} + \text{R.T.}, \qquad \mathbf{j} \in \Gamma_h, \tag{22}$$

and this result for $\mathbf{E}_{\mathbf{j}}^{n+1}$ can be used in (20b) to give

$$\mathbf{P}_{m,\mathbf{j}}^{n+1} = \frac{\tilde{a}_{1,m}\Delta t/2}{1 + b_{1,m}\Delta t/2}\left(\frac{(c\Delta t)^2}{1+\beta\epsilon_0^{-1}}\right)\Delta_{2h}\mathbf{E}_{\mathbf{j}}^{n} + \text{R.T.}, \qquad \mathbf{j} \in \Gamma_h, \tag{23}$$

Second-order accurate approximations for the first derivatives of $\mathbf{E}$ and $\mathbf{P}_m$ are

$$\partial_t \mathbf{E}\big|_{\mathbf{j}}^{n} = D_{0t}\mathbf{E}_{\mathbf{j}}^{n} = \frac{\Delta t}{2}\left(\frac{c^2}{1+\beta\epsilon_0^{-1}}\right)\Delta_{2h}\mathbf{E}_{\mathbf{j}}^{n} + \text{R.T.}, \qquad \mathbf{j} \in \Gamma_h, \tag{24a}$$

$$\partial_t \mathbf{P}_m\big|_{\mathbf{j}}^{n} = D_{0t}\mathbf{P}_{m,\mathbf{j}}^{n} = \frac{\Delta t}{2}\,\frac{\tilde{a}_{1,m}\Delta t/2}{1 + b_{1,m}\Delta t/2}\left(\frac{c^2}{1+\beta\epsilon_0^{-1}}\right)\Delta_{2h}\mathbf{E}_{\mathbf{j}}^{n} + \text{R.T.}, \qquad \mathbf{j} \in \Gamma_h, \tag{24b}$$

using the expressions for $\mathbf{E}_{\mathbf{j}}^{n+1}$ and $\mathbf{P}_{m,\mathbf{j}}^{n+1}$ in (22) and (23), respectively. A second-order accurate approximation of the governing equation for $\mathbf{P}_m$ in (3b) at time t^n is

$$\partial_t^2 \mathbf{P}_m\big|_{\mathbf{j}}^{n} = -b_{1,m}\partial_t \mathbf{P}_m\big|_{\mathbf{j}}^{n} - b_{0,m}\mathbf{P}_{m,\mathbf{j}}^{n} + \tilde{a}_{0,m}\mathbf{E}_{\mathbf{j}}^{n} + \tilde{a}_{1,m}\partial_t\mathbf{E}\big|_{\mathbf{j}}^{n}, \qquad \mathbf{j} \in \Gamma_h, \tag{25}$$

Using the approximations in (24) for the first deriatives of $\mathbf{E}$ and $\mathbf{P}_m$ in (25), and then summing over m, gives

$$\partial_t^2 \mathbf{P}\big|_{\mathbf{j}}^{n} = \left(\frac{\beta c^2}{1+\beta\epsilon_0^{-1}}\right)\Delta_{2h}\mathbf{E}_{\mathbf{j}}^{n} + \text{R.T.}, \qquad \mathbf{j} \in \Gamma_h, \tag{26}$$

which has the form of (19) with $K_0^{\partial_t^2\mathbf{P}} = \beta c^2/(1+\beta\epsilon_0^{-1})$.

Summary: The ghost point values at the interface for the second-order accurate scheme are determined by the solution to the following equations:

$$\left[\mathbf{n} \times \left(c^2\Delta_{2h}\mathbf{E}_{\mathbf{j}}^{n} - \epsilon_0^{-1}K^{\partial_t^2\mathbf{P}}\Delta_{2h}\mathbf{E}_{\mathbf{j}}^{n}\right)\right]_I = [\text{R.T.}]_I\,, \qquad \mathbf{j} \in \Gamma_h, \tag{27a}$$

$$\left[\mu_0^{-1}\mathbf{n}\cdot\Delta_{2h}\mathbf{E}_{\mathbf{j}}^{n}\right]_I = 0, \qquad \mathbf{j} \in \Gamma_h, \tag{27b}$$

$$\left[\mu_0^{-1}\mathbf{n}\times\nabla_{2h}\times\mathbf{E}^n_{\mathbf{j}}\right]_I = 0, \qquad \mathbf{j}\in\Gamma_h, \tag{27c}$$

$$\left[\nabla_{2h}\cdot\mathbf{E}^n_{\mathbf{j}}\right]_I = 0, \qquad \mathbf{j}\in\Gamma_h, \tag{27d}$$

where $K_0^{\partial_t^2\mathbf{P}}$ is defined in (26) and $[\text{R.T.}]_I$ in (27a) is given by

$$[\text{R.T.}]_I = \left[\mathbf{n}\times\epsilon_0^{-1}\left\{c_0\,\mathbf{E}^n_{\mathbf{j}} + c_1\,\mathbf{E}^{n-1}_{\mathbf{j}} + \sum_{m=1}^{N_p}\left(d_{0,m}\,\mathbf{P}^n_{m,\mathbf{j}} + d_{1,m}\,\mathbf{P}^{n-1}_{m,\mathbf{j}}\right)\right\}\right]_I, \tag{28}$$

for the constants $\{c_0, c_1\}$ and $\{d_{0,m}, d_{1,m}\}$, $m = 1, 2, \dots, N_p$, in (19) defined on either side of the interface (and given in the CgMx distribution).

4.2. Fourth-order accurate interface approximations

The fourth-order accurate time-stepping scheme in (13) requires two ghost points on each side of the interface, and so additional compatability equations are needed on top of the ones used for the second-order scheme. The starting point for the derivation of the new conditions is the previous set of interface conditions given by the derived conditions in (16a) and (16b) and the primary interface conditions in (8c) and (8d). Taking two derivatives with respect to time of each of these four conditions, and using derivatives of the governing equations in (3), leads to four additional interface conditions given by

$$\left[\mathbf{n}\times\left(c^4\Delta^2\mathbf{E} - c^2\epsilon_0^{-1}\Delta\partial_t^2\mathbf{P} - \epsilon_0^{-1}\partial_t^4\mathbf{P}\right)\right]_I = 0, \qquad \mathbf{x}\in\Gamma, \tag{29a}$$

$$\left[\mu_0^{-1}\mathbf{n}\cdot\left(c^2\Delta^2\mathbf{E} - \epsilon_0^{-1}\Delta\partial_t^2\mathbf{P}\right)\right]_I = 0, \qquad \mathbf{x}\in\Gamma, \tag{29b}$$

$$\left[\mu_0^{-1}\mathbf{n}\times\nabla\times\left(c^2\Delta\mathbf{E} - \epsilon_0^{-1}\partial_t^2\mathbf{P}\right)\right]_I = 0, \qquad \mathbf{x}\in\Gamma, \tag{29c}$$

$$\left[c^2\nabla\cdot(\Delta\mathbf{E})\right]_I = 0, \qquad \mathbf{x}\in\Gamma. \tag{29d}$$

Note that $\nabla\cdot\mathbf{P} = 0$ has been used in the derivation of (29d).

Approximations of the original four interface conditions, and the four new conditions in (29), suitable for the fourth-order accurate time-stepping scheme are given by

$$\left[\mathbf{n}\times\left(c^2\Delta_{4h}\mathbf{E}^n_{\mathbf{j}} - \epsilon_0^{-1}\partial_t^2\mathbf{P}\big|^n_{\mathbf{j}}\right)\right]_I = 0, \qquad \mathbf{j}\in\Gamma_h, \tag{30a}$$

$$\left[\mu_0^{-1}\mathbf{n}\cdot\Delta_{4h}\mathbf{E}^n_{\mathbf{j}}\right]_I = 0, \qquad \mathbf{j}\in\Gamma_h, \tag{30b}$$

$$\left[\mu_0^{-1}\mathbf{n}\times\left(\nabla_{4h}\times\mathbf{E}^n_{\mathbf{j}}\right)\right]_I = 0, \qquad \mathbf{j}\in\Gamma_h, \tag{30c}$$

$$\left[\nabla_{4h}\cdot\mathbf{E}^n_{\mathbf{j}}\right]_I = 0, \qquad \mathbf{j}\in\Gamma_h, \tag{30d}$$

$$\left[\mathbf{n}\times\left(c^4\Delta_{2h}^2\mathbf{E}^n_{\mathbf{j}} - c^2\epsilon_0^{-1}\,\Delta_{2h}\partial_t^2\mathbf{P}^*\big|^n_{\mathbf{j}} - \epsilon_0^{-1}\partial_t^4\mathbf{P}^*\big|^n_{\mathbf{j}}\right)\right]_I = 0, \qquad \mathbf{j}\in\Gamma_h, \tag{30e}$$

$$\left[\mu_0^{-1}\mathbf{n}\cdot\left(c^2\Delta_{2h}^2\mathbf{E}^n_{\mathbf{j}} - \epsilon_0^{-1}\Delta_{2h}\partial_t^2\mathbf{P}^*\big|^n_{\mathbf{j}}\right)\right]_I = 0, \qquad \mathbf{j}\in\Gamma_h, \tag{30f}$$

$$\left[\mu_0^{-1}\mathbf{n}\times\left(c^2\nabla_{2h}\times\Delta_{2h}\mathbf{E}^n_{\mathbf{j}} - \epsilon_0^{-1}\nabla_{2h}\times\partial_t^2\mathbf{P}^*\big|^n_{\mathbf{j}}\right)\right]_I = 0, \qquad \mathbf{j}\in\Gamma_h, \tag{30g}$$

$$\left[c^2\nabla_{2h}\cdot\left(\Delta_{2h}\mathbf{E}^n_{\mathbf{j}}\right)\right]_I = 0, \qquad \mathbf{j}\in\Gamma_h, \tag{30h}$$

where ∇_{4h} and Δ_{4h} denote fourth-order accurate approximations (with a five-point stencil in each coordinate direction) to the gradient and Laplace operators, respectively. Note that the compatibility conditions in (29) involve third and fourth-order spatial derivatives, whereas the original set of interface conditions involve only first and second-order derivatives. The corresponding approximations of these higher derivatives in (30e)–(30h) require only second-order accurate approximations, whereas fourth-order accurate approximation are used in (30a)–(30d). This is a typical approach in the approximation of compatibility conditions, and it results here in a fourth-order approximation of the overall time-stepping scheme. A general rule of thumb is that the discrete approximations at an interface and/or boundary of the grid should never require a larger stencil than the basic scheme used in the interior.

It remains to describe approximations for the terms involving the temporal derivatives of $\mathbf{P}$ in (30). In keeping with the aforementioned rule of thumb, a fourth-order accurate approximation is needed for $\partial_t^2\mathbf{P}\big|_{\mathbf{j}}^n$ in (30a), while only second-order accurate approximations are required for $\Delta_{2h}\partial_t^2\mathbf{P}^*\big|_{\mathbf{j}}^n$, $\nabla_{2h}\times\partial_t^2\mathbf{P}^*\big|_{\mathbf{j}}^n$ and $\partial_t^4\mathbf{P}^*\big|_{\mathbf{j}}^n$ in (30e)–(30g). (Magenta is used to highlight terms that are fourth-order accurate, while blue is still used to highlight second-order accurate terms with the asterisk indicating terms that are obtained from the imbedded second-order accurate scheme in Algorithm 2.) As before, we seek expressions for all of these terms as linear combinations of approximations of spatial derivatives of $\mathbf{E}_{\mathbf{j}}^n$ (which involve the one or two ghost values of interest) together with known values for $\mathbf{E}_{\mathbf{j}}^n$, $\mathbf{E}_{\mathbf{j}}^{n-1}$, $\mathbf{P}_{m,\mathbf{j}}^n$ and $\mathbf{P}_{m,\mathbf{j}}^{n-1}$ on the interface, and perhaps approximations of other spatial derivatives which are also considered to be known. For example, a suitable formula for $\partial_t^2\mathbf{P}\big|_{\mathbf{j}}^n$ takes the form

$$\begin{aligned}\partial_t^2\mathbf{P}\big|_{\mathbf{j}}^n = {}& K_1^{\partial_t^2\mathbf{P}}\Delta_{2h}\mathbf{E}_{\mathbf{j}}^n + K_2^{\partial_t^2\mathbf{P}}\Delta_{2h}^2\mathbf{E}_{\mathbf{j}}^n + K_4^{\partial_t^2\mathbf{P}}\Delta_{4h}\mathbf{E}_{\mathbf{j}}^n + c_0\,\mathbf{E}_{\mathbf{j}}^n + c_1\,\mathbf{E}_{\mathbf{j}}^{n-1} + c_2\,\Delta_{4h}\mathbf{E}_{\mathbf{j}}^{n-1} \\ &+ \sum_{m=1}^{N_p}\Big(d_{0,m}\,\mathbf{P}_{m,\mathbf{j}}^n + d_{1,m}\,\mathbf{P}_{m,\mathbf{j}}^{n-1} + d_{2,m}\,\Delta_{4h}\mathbf{P}_{m,\mathbf{j}}^n + d_{3,m}\,\Delta_{4h}\mathbf{P}_{m,\mathbf{j}}^{n-1}\Big),\end{aligned} \tag{31}$$

where $K_1^{\partial_t^2\mathbf{P}}$, $K_2^{\partial_t^2\mathbf{P}}$, $K_4^{\partial_t^2\mathbf{P}}$, $\{c_0, c_1, c_2\}$ and $\{d_{0,m}, d_{1,m}, d_{2,m}, d_{3,m}\}$, $m = 1, 2, \ldots, N_p$, are constants. Note that the expression in (31) requires $\Delta_{4h}\mathbf{P}_{m,\mathbf{j}}^n$ and $\Delta_{4h}\mathbf{P}_{m,\mathbf{j}}^{n-1}$ on the interface. Since there are no explicit interface conditions on $\mathbf{P}$, these spatial derivatives are approximated using one-sided finite-difference formulas. As in the previous case, we focus our attention on the dependence of $\Delta_{2h}\mathbf{E}_{\mathbf{j}}^n$, $\Delta_{2h}^2\mathbf{E}_{\mathbf{j}}^n$ and $\Delta_{4h}\mathbf{E}_{\mathbf{j}}^n$ (which involve ghost points) and lump the other (known) terms into a remainder term, so that (31) becomes

$$\partial_t^2\mathbf{P}\big|_{\mathbf{j}}^n = K_1^{\partial_t^2\mathbf{P}}\Delta_{2h}\mathbf{E}_{\mathbf{j}}^n + K_2^{\partial_t^2\mathbf{P}}\Delta_{2h}^2\mathbf{E}_{\mathbf{j}}^n + K_4^{\partial_t^2\mathbf{P}}\Delta_{4h}\mathbf{E}_{\mathbf{j}}^n + \text{R.T.}, \tag{32}$$

for ease of discussion.

A fourth-order accurate formula for $\partial_t^2\mathbf{P}\big|_{\mathbf{j}}^n$, in the form of (32), can be found by following steps similar to the ones taken to determine the second-order accurate formula in (26). Here, we consider the fourth-order accurate approximations of the governing equations in (13) for $\mathbf{j}\in\Gamma_h$. Upon multiplication by Δt^2, these equations take the form

$$\mathbf{E}_{\mathbf{j}}^{n+1} + \frac{1}{\epsilon_0}\mathbf{P}_{\mathbf{j}}^{n+1} = K_{11}\Delta_{2h}\mathbf{E}_{\mathbf{j}}^n + K_{12}\Delta_{2h}^2\mathbf{E}_{\mathbf{j}}^n + (c\Delta t)^2\Delta_{4h}\mathbf{E}_{\mathbf{j}}^n + \text{R.T.}, \tag{33a}$$

$$-\frac{\tilde{a}_{1,m}\Delta t}{2}\mathbf{E}_{\mathbf{j}}^{n+1} + \left(1 + \frac{b_{1,m}\Delta t}{2}\right)\mathbf{P}_{m,\mathbf{j}}^{n+1} = K_{21,m}\Delta_{2h}\mathbf{E}_{\mathbf{j}}^n + K_{22,m}\Delta_{2h}^2\mathbf{E}_{\mathbf{j}}^n + \text{R.T.}, \tag{33b}$$

where K_{11}, K_{12}, $K_{21,m}$ and $K_{22,m}$ are constants. The system in (33) for $\mathbf{E}_{\mathbf{j}}^{n+1}$ and $\mathbf{P}_{m,\mathbf{j}}^{n+1}$ is similar to the one in (20) for the second-order case, but it has additional terms on the right-hand side involving $\Delta_{2h}\mathbf{E}_{\mathbf{j}}^{n}$ and $\Delta_{2h}^{2}\mathbf{E}_{\mathbf{j}}^{n}$ that arise from approximations of the blue-highlighted terms in (13) as described below. As before, we solve (33b) for $\mathbf{P}_{m,\mathbf{j}}^{n+1}$ and then sum over m to give

$$\mathbf{P}_{\mathbf{j}}^{n+1} = \beta\mathbf{E}_{\mathbf{j}}^{n+1} + K_{21}\Delta_{2h}\mathbf{E}_{\mathbf{j}}^{n} + K_{22}\Delta_{2h}^{2}\mathbf{E}_{\mathbf{j}}^{n} + \text{R.T.}, \tag{34}$$

where K_{21} and K_{22} are constants (related to $K_{21,m}$ and $K_{22,m}$ above) and β is the same constant appearing in (21). Equation (34) can be used to eliminate $\mathbf{P}_{\mathbf{j}}^{n+1}$ in (33a), and then the system in (33) can be solved for $\mathbf{E}_{\mathbf{j}}^{n+1}$ and $\mathbf{P}_{m,\mathbf{j}}^{n+1}$. Expressions for these quantities have the form

$$\mathbf{E}_{\mathbf{j}}^{n+1} = \tilde{K}_{11}\Delta_{2h}\mathbf{E}_{\mathbf{j}}^{n} + \tilde{K}_{12}\Delta_{2h}^{2}\mathbf{E}_{\mathbf{j}}^{n} + \tilde{K}_{14}\Delta_{4h}\mathbf{E}_{\mathbf{j}}^{n} + \text{R.T.}, \tag{35a}$$

$$\mathbf{P}_{m,\mathbf{j}}^{n+1} = \tilde{K}_{21,m}\Delta_{2h}\mathbf{E}_{\mathbf{j}}^{n} + \tilde{K}_{22,m}\Delta_{2h}^{2}\mathbf{E}_{\mathbf{j}}^{n} + \tilde{K}_{24,m}\Delta_{4h}\mathbf{E}_{\mathbf{j}}^{n} + \text{R.T.}, \tag{35b}$$

where $\tilde{K}_{q1}$, $\tilde{K}_{q2}$ and $\tilde{K}_{q4}$, $q = 1, 2$, are constants. Fourth-order accurate approximations for the first derivatives of $\mathbf{E}$ and $\mathbf{P}_m$ are given by

$$\partial_t\mathbf{E}\big|_{\mathbf{j}}^{n} = D_{0t}\mathbf{E}_{\mathbf{j}}^{n} - \frac{\Delta t^2}{3!}\partial_t^3\mathbf{E}^*\big|_{\mathbf{j}}^{n}, \tag{36a}$$

$$\partial_t\mathbf{P}_m\big|_{\mathbf{j}}^{n} = D_{0t}\mathbf{P}_{m,\mathbf{j}}^{n} - \frac{\Delta t^2}{3!}\partial_t^3\mathbf{P}_m^*\big|_{\mathbf{j}}^{n}, \tag{36b}$$

where D_{0t} is the centered first divided difference operator, and $\partial_t^3\mathbf{E}^*\big|_{\mathbf{j}}^{n}$ and $\partial_t^3\mathbf{P}_m^*\big|_{\mathbf{j}}^{n}$ are second-order accurate approximations for the third derivatives of $\mathbf{E}$ and $\mathbf{P}_m$, respectively. The expressions for $\mathbf{E}_{\mathbf{j}}^{n+1}$ and $\mathbf{P}_{m,\mathbf{j}}^{n+1}$ in (35), along with known values at t^{n-1}, can be used to evaluate the divided differences in (36), while approximations for the third derivatives can be obtained from the governing equations in (3) upon differentiation with respect to time. For example, taking the derivative of (3b), and using (3a) and (3b) to eliminate the second derivatives of $\mathbf{E}$ and $\mathbf{P}_m$, respectively, gives

$$\begin{aligned}\partial_t^3\mathbf{P}_m = {}& -b_{1,m}\big(-b_{1,m}\partial_t\mathbf{P}_m - b_{0,m}\mathbf{P} + \tilde{a}_{0,m}\mathbf{E} + \tilde{a}_{1,m}\partial_t\mathbf{E}\big) - b_{0,m}\partial_t\mathbf{P}_m \\ & + \tilde{a}_{0,m}\partial_t\mathbf{E} + \tilde{a}_{1,m}\Big(c^2\Delta\mathbf{E} - \epsilon_0^{-1}\sum_m\big(-b_{1,m}\partial_t\mathbf{P}_m - b_{0,m}\mathbf{P}_m + \tilde{a}_{0,m}\mathbf{E} + \tilde{a}_{1,m}\partial_t\mathbf{E}\big)\Big).\end{aligned} \tag{37}$$

Using (24) to approximate the first derivatives of $\mathbf{E}$ and $\mathbf{P}_m$ in (37), and a similar expression for $\partial_t^3\mathbf{E}$, and using a second-order accurate approximation for the Laplacian, leads to formulas for the third derivatives of the form

$$\partial_t^3\mathbf{E}^*\big|_{\mathbf{j}}^{n} = K^{\partial_t^3\mathbf{E}}\Delta_{2h}\mathbf{E}_{\mathbf{j}}^{n} + \text{R.T.}, \tag{38a}$$

$$\partial_t^3\mathbf{P}_m^*\big|_{\mathbf{j}}^{n} = K^{\partial_t^3\mathbf{P}_m}\Delta_{2h}\mathbf{E}_{\mathbf{j}}^{n} + \text{R.T.}, \tag{38b}$$

where $K^{\partial_t^3\mathbf{E}}$ and $K^{\partial_t^3\mathbf{P}_m}$ are constants. The approximations in (38) are used in (36), along with the first divided differences of $\mathbf{E}$ and $\mathbf{P}_m$, to give the fourth-order accurate approximations

$$\partial_t\mathbf{E}\big|_{\mathbf{j}}^{n} = K_1^{\partial_t\mathbf{E}}\Delta_{2h}\mathbf{E}_{\mathbf{j}}^{n} + K_2^{\partial_t\mathbf{E}}\Delta_{2h}^{2}\mathbf{E}_{\mathbf{j}}^{n} + K_4^{\partial_t\mathbf{E}}\Delta_{4h}\mathbf{E}_{\mathbf{j}}^{n} + \text{R.T.} \tag{39a}$$

$$\partial_t \mathbf{P}_m\big|_{\mathbf{j}}^n = K_1^{\partial_t \mathbf{P}_m} \Delta_{2h} \mathbf{E}_{\mathbf{j}}^n + K_2^{\partial_t \mathbf{P}_m} \Delta_{2h}^2 \mathbf{E}_{\mathbf{j}}^n + K_4^{\partial_t \mathbf{P}_m} \Delta_{4h} \mathbf{E}_{\mathbf{j}}^n + \text{R.T.}, \tag{39b}$$

Following the steps before, we use the governing equation for $\mathbf{P}_m$ and the approximations of the first derivatives in (39) to obtain a fourth-order accurate approximation for $\partial_t^2 \mathbf{P}_m$. Summing this approximation over m gives an expression of the form

$$\partial_t^2 \mathbf{P}\big|_{\mathbf{j}}^n = K_1^{\partial_t^2 \mathbf{P}} \Delta_{2h} \mathbf{E}_{\mathbf{j}}^n + K_2^{\partial_t^2 \mathbf{P}} \Delta_{2h}^2 \mathbf{E}_{\mathbf{j}}^n + K_4^{\partial_t^2 \mathbf{P}} \Delta_{4h} \mathbf{E}_{\mathbf{j}}^n + \text{R.T.}, \tag{40}$$

where $K_1^{\partial_t^2 \mathbf{P}}$, $K_2^{\partial_t^2 \mathbf{P}}$ and $K_4^{\partial_t^2 \mathbf{P}}$ are constants.

We next derive formulas for the second-order accurate terms $\Delta_{2h} \partial_t^2 \mathbf{P}^*\big|_{\mathbf{j}}^n$ and $\nabla_{2h} \times \partial_t^2 \mathbf{P}^*\big|_{\mathbf{j}}^n$. We recall that the fourth-order accurate time-stepping scheme in Algorithm 2 uses second-order accurate approximations for $\mathbf{E}$ and $\mathbf{P}$ at t^{n+1}, denoted with star superscripts, as a means to evaluate the blue highlighted terms in the fourth-order accurate approximations of the governing equations in (13). In terms of the linear combinations of interest, we note that a second-order accurate expression for $\partial_t^2 \mathbf{P}\big|_{\mathbf{j}}^n$ appeared before in (26). Using this expression, we apply the discrete Laplacian and curl operators to give

$$\Delta_{2h} \partial_t^2 \mathbf{P}^*\big|_{\mathbf{j}}^n = K_0^{\partial_t^2 \mathbf{P}} \Delta_{2h}^2 \mathbf{E}_{\mathbf{j}}^n + K_1^{\Delta \partial_t^2 \mathbf{P}} \Delta_{2h} \mathbf{E}_{\mathbf{j}}^n + \text{R.T.}, \tag{41a}$$

$$\nabla_{2h} \times \partial_t^2 \mathbf{P}^*\big|_{\mathbf{j}}^n = K_0^{\partial_t^2 \mathbf{P}} \nabla_{2h} \times \Delta_{2h} \mathbf{E}_{\mathbf{j}}^n + K_1^{\nabla \times \partial_t^2 \mathbf{P}} \nabla_{2h} \times \mathbf{E}_{\mathbf{j}}^n + \text{R.T.}, \tag{41b}$$

where $K_0^{\partial_t^2 \mathbf{P}}$, $K_1^{\Delta \partial_t^2 \mathbf{P}}$ and $K_1^{\nabla \times \partial_t^2 \mathbf{P}}$ are constants and $\mathbf{j} \in \Gamma_h$. Note that the coefficient, $K_0^{\partial_t^2 \mathbf{P}}$, of the leading terms in (41a) and (41b) is the same one in (26), and that the terms with coefficients, $K_1^{\Delta \partial_t^2 \mathbf{P}}$ and $K_1^{\nabla \times \partial_t^2 \mathbf{P}}$, arise from the discrete Laplacian and curl operators applied to the term involving $\mathbf{E}_{\mathbf{j}}^n$ in the remainder term of (26).

The last task involves the derivation of a formula for $\partial_t^4 \mathbf{P}^*\big|_{\mathbf{j}}^n$, which is needed by the interface condition in (30e). A formula for this term can obtained by using the governing equations in (3) to write $\partial_t^4 \mathbf{P}_m$ in terms of the $\mathbf{E}$, $\partial_t \mathbf{E}$, $\mathbf{P}_m$ and $\partial_t \mathbf{P}_m$, and their spatial derivatives. Using the second-order accurate approximations for the first derivatives in (24) leads to an expression for $\partial_t^4 \mathbf{P}_m^*\big|_{\mathbf{j}}^n$ of the form

$$\partial_t^4 \mathbf{P}_m^*\big|_{\mathbf{j}}^n = K_1^{\partial_t^4 \mathbf{P}_m} \Delta_{2h} \mathbf{E}_{\mathbf{j}}^n + K_2^{\partial_t^4 \mathbf{P}_m} \Delta_{2h}^2 \mathbf{E}_{\mathbf{j}}^n + \text{R.T.}, \tag{42}$$

where $K_1^{\partial_t^4 \mathbf{P}_m}$ and $K_2^{\partial_t^4 \mathbf{P}_m}$ are constants. Summing the expression in (42) over m gives the required result

$$\partial_t^4 \mathbf{P}^*\big|_{\mathbf{j}}^n = K_1^{\partial_t^4 \mathbf{P}} \Delta_{2h} \mathbf{E}_{\mathbf{j}}^n + K_2^{\partial_t^4 \mathbf{P}} \Delta_{2h}^2 \mathbf{E}_{\mathbf{j}}^n + \text{R.T.}, \tag{43}$$

where $K_q^{\partial_t^4 \mathbf{P}} = \sum_m K_q^{\partial_t^4 \mathbf{P}_m}$, $q = 1$ and 2.

Summary: The ghost point values at the interface for the fourth-order accurate scheme are determined by the solution of the jump conditions in (30), where $\partial_t^2 \mathbf{P}\big|_{\mathbf{j}}^n$, $\Delta_{2h} \partial_t^2 \mathbf{P}^*\big|_{\mathbf{j}}^n$, $\nabla_{2h} \times \partial_t^2 \mathbf{P}^*\big|_{\mathbf{j}}^n$ and $\partial_t^4 \mathbf{P}^*\big|_{\mathbf{j}}^n$ are determined by the formulas given in (40), (41a), (41b) and (43), respectively, which are linear combinations of spatial approximations (involving the ghost points) and known grid values at time levels t^n and t^{n-1}.

4.3. Decoupling the interface equations in tangential directions

We now describe an efficient approach to approximately solve the interface equations in (17) for the second-order accurate scheme, or in (30) for the fourth-order accurate scheme. This approach approximately eliminates any coupling in the tangential directions, and thus avoids the solution to a large system of equations at each time step involving the solution values at all ghost points adjacent to the interface. Only small systems of equations involving the solution components at ghost points adjacent to each interface point need be solved.

To better understand the issue of tangential coupling, let us start by considering the form of $\Delta_{2h}\mathbf{E}_{\mathbf{j}}^n$ that appears in the interface conditions in (17) for the second-order accurate scheme. In general curvilinear coordinates $\mathbf{x} = \mathbf{G}(\mathbf{r})$ in two dimensions, the Laplace operator can be written using the chain rule in non-conservative form as (similar issues occur for the conservative form)

$$\Delta u = c_{11}(r,s)\,\partial_r^2 U + c_{12}(r,s)\,\partial_r\partial_s U + c_{22}(r,s)\,\partial_s^2 U + c_1(r,s)\,\partial_r U + c_2(r,s)\,\partial_s U, \tag{44}$$

where $\mathbf{r} = (r,s)$, and $u(x,y) = U(r,s)$ represents a component of $\mathbf{E}$. For an interface comforming grid let us assume the interface is at $r = 0$ and that s varies in the tangential direction to the interface. The problematic term in (44) that introduces coupling in the tangential direction is the mixed-derivative term $c_{12}(r,s)\partial_r\partial_s U$, which at second-order is approximated using

$$\partial_r\partial_s U \approx D_{0r}D_{0s}U_{\mathbf{j}} = \frac{1}{4\Delta r\Delta s}\Big[U_{j_1+1,j_2+1} - U_{j_1-1,j_2+1} - U_{j_1+1,j_2-1} + U_{j_1-1,j_2-1}\Big],$$

where D_{0r} and D_{0s} are the central difference operators in the r and s directions, respectively. On an orthogonal grid, $c_{12} = 0$, and there is no mixed-derivative term and subsequently no tangential coupling. When the grid is not orthogonal, however, $c_{12} \neq 0$ and the mixed-derivative term is present, and coupling in the tangential direction occurs. To avoid dealing with the coupling arising from this term, we assume the grid close to the boundary is nearly orthogonal (this is an advisable grid generation rule of thumb), and thus c_{12} is assumed to be small as compared to c_{11}. In this case the mixed derivative terms are treated with one-sided difference approximations, which can be implemented in practice by first extrapolating the ghost point values and then evaluating the centered difference approximation to $\partial_r\partial_s U$. This approach is always accurate and thus the only concern with this approximation is whether the scheme remains stable. In practice this approach has worked well over a wide range of cases.

The interface equations in (30) for the fourth-order accurate scheme also have mixed-derivative terms in $\Delta_{4h}\mathbf{E}_{\mathbf{j}}^n$, for example, that can be approximated to fourth-order accuracy using one-sided difference approximations. However, the fourth-order accurate interface conditions also have higher-order mixed-derivative terms such as the term $\partial_x^2\partial_y^2\mathbf{E}$ that appears in $\Delta^2\mathbf{E}$ as

$$\Delta^2\mathbf{E} = \partial_x^4\mathbf{E} + 2\partial_x^2\partial_y^2\mathbf{E} + \partial_y^4\mathbf{E},$$

for the case of two dimensions. For this derivative, there is a mixed-derivative term with a coefficient that is not small (as in the case of the mapped Laplacian for a nearly orthogonal grid). Fortunately this term need only be approximated to second-order accuracy. We have found that an effective way to approximate these mixed-derivative terms is to first apply the second-order accurate interface conditions from Section 4.1 to obtain predicted values for the first line of ghost points adjacent to the interface. These predicted values can subsequently be used to approximate the mixed-derivative term $\partial_x^2\partial_y^2\mathbf{E}$ to second-order accuracy.

For curvilinear grids, all mixed-derivative terms that appear in the curvilinear coordinate approximations to (30) are thus approximated to either fourth-order or second-order accuracy using one-side approximations or predicted values from the second-order accurate interface conditions. As a result, the solution values at ghost points are decoupled in the tangential direction and thus the ghost-point values at the interface can be evaluated using local approximations that require the solution to small systems of equations involving $4n_d$ unknowns (4 total ghost points values of $\mathbf{E}$ for fourth-order accuracy) at each interface point.

We make a final remark that one should generally always use the decoupling procedure when solving the fourth-order interface equations as there appears to be cases when the solution of the original coupled equations lead to an unstable scheme in time. The problematic situation seems to be when there are *tall* grid cells at the interface (i.e. cells where the grid-spacing Δr is larger than the grid spacing Δs in the tangential direction). A more detailed analysis of this issue is left to a future paper.

4.4. Interface projection

The primary interface jump conditions in (8a) and (8b) are not imposed explicitly when solving for the ghost point values at the interface, only the second time derivative of these conditions are imposed as in (16a) and (16b). If the primary conditions are satisfied initially, then they would be satisfied for all time in the exact solution by imposing (16a) and (16b). At a discrete level, however, the primary conditions would only be satisfied approximately. To strictly enforce the primary interface jump conditions at a discrete level, we apply an interface projection at each time-step before assigning the ghost values.

We consider the solution of a Riemann problem centered at the interface in a direction normal to the interface to define the projection. The initial condition for the Riemann problem, taken at a pseudo-time $t = 0$, consists of a constant left state for $x < 0$ and a constant right state for $x > 0$, where x measures distance normal to the interface. The values for these left and right states are given by the predicted interface values coming from the left and right interior updates on the interface. The central state in the solution of the Riemann problem at $x = 0$ and at an infinitesimal positive time $t = 0+$ is taken as the projected interface state.

To derive the form of the projected state, it is sufficient to consider Maxwell's equations in two dimensions for a TE-z polarized wave. Taking $u = E_x(x,t)$, $v = E_y(x,t)$ and $w = H_z(x,t)$, we consider the system

$$\partial_t\big(\epsilon_0 u + p\big) = \partial_y w, \tag{45a}$$

$$\partial_t\big(\epsilon_0 v + q\big) = -\partial_x w, \tag{45b}$$

$$\mu_0 \partial_t w = \partial_y u - \partial_x v, \tag{45c}$$

where the polarization variables p and q are assumed to satisfy scalar versions of the auxiliary differential equations in (3b). Considering the system in (45) in the x-direction (normal direction) gives

$$\partial_t\big(\epsilon_0 u + p\big) = 0, \tag{46a}$$

$$\partial_t\big(\epsilon_0 v + q\big) = -\partial_x w, \tag{46b}$$

$$\mu_0 \partial_t w = -\partial_x v. \tag{46c}$$

Equation (46a) is already in characteristic form and this is used to obtain a projected value for u as described below. It is straightforward to show that the polarization variable q in (46b) acts as a lower-order term, which can be neglected in a characteristic analysis since we are only interested in the solution at $t = 0+$. Under this assumption, the characteristic equations corresponding to (46b) and (46c) are

$$\frac{d}{dt}(v \pm \eta w) = 0, \qquad \text{on} \quad \frac{dx}{dt} = \pm c, \tag{47}$$

where $c = 1/\sqrt{\epsilon_0 \mu_0}$ is the wave speed and $\eta = \mu_0 c$ is the electric impedance. Let subscripts L and R denote quantities in the left and right states, respectively. Solving the Riemman problem with the interface jump conditions

$$[v]_I = [w]_I = 0,$$

leads to the central state, denoted by (v^I, w^I), given by

$$v^I = \frac{\eta_L^{-1} v_L + \eta_R^{-1} v_R}{\eta_R^{-1} + \eta_L^{-1}} - \frac{w_R - w_L}{\eta_R^{-1} + \eta_L^{-1}}, \tag{48a}$$

$$w^I = \frac{\eta_R w_R + \eta_L w_L}{\eta_R + \eta_L} - \frac{v_R - v_L}{\eta_R + \eta_L}. \tag{48b}$$

The terms in (48) involving the differences of v and w in the left and right states can be neglected since they are usually proportional to the truncation error. With these terms omitted, we observe that v^I is given by an inverse impedance average, while w^I is given by an impedance average.

The interface treatment of the normal component of the electric displacement, $\mathbf{n} \cdot \mathbf{D}$, taken here as $\epsilon_0 u + p$ is less straightforward since its characteristic equation (46a) is parallel to the interface. For this case, we propose a heuristic projection. Given left state $D_L \overset{\text{def}}{=} \epsilon_{0,L} u_L + p_L$ and right state $D_R \overset{\text{def}}{=} \epsilon_{0,R} u_R + p_R$, we set the interface value D^I to be the state with corresponding smaller permittivity,

$$D^I = \begin{cases} D_L, & \text{if } \epsilon_{0,L} \leqslant \epsilon_{0,R}, \\ D_R, & \text{if } \epsilon_{0,R} < \epsilon_{0,L}. \end{cases} \tag{49}$$

Thus, if $\epsilon_{0,L} \leqslant \epsilon_{0,R}$, we take $D^I = D_L$, which implies $u_L^I = u_L$ and

$$u_R^I = \frac{D^I - p_R}{\epsilon_{0,R}} = \left(\frac{\epsilon_{0,L}}{\epsilon_{0,R}}\right) u_L + \frac{p_L - p_R}{\epsilon_{0,R}}. \tag{50a}$$

Otherwise, $D^I = D_R$, which implies $u_R^I = u_R$ and

$$u_L^I = \frac{D^I - p_L}{\epsilon_{0,L}} = \left(\frac{\epsilon_{0,R}}{\epsilon_{0,L}}\right) u_R + \frac{p_R - p_L}{\epsilon_{0,L}}. \tag{50b}$$

The intuition for this choice is based on a numerical stability argument. If $\epsilon_{0,L} \leqslant \epsilon_{0,R}$, then the interface value given by u_R^I in (50a) is not amplified by a perturbation to $u_L \to u_L + \delta$ (e.g. round-off errors) since $(\epsilon_{0,L}/\epsilon_{0,R}) \leqslant 1$. Likewise, the modification to u_L^I in (50b) does not amplify perturbations in u_R since $(\epsilon_{0,R}/\epsilon_{0,L}) < 1$.

Summary. The tangential components of the electric field are projected using an inverse impedance weighted average,

$$(\mathbf{n}\times\mathbf{E})^I = \frac{\eta_L^{-1}(\mathbf{n}\times\mathbf{E})_L + \eta_R^{-1}(\mathbf{n}\times\mathbf{E})_R}{\eta_L^{-1}+\eta_R^{-1}},$$

where $\eta_\xi = \sqrt{\mu_{0,\xi}/\epsilon_{0,\xi}}$. The normal component of the field is projected using

$$(\mathbf{n}\cdot\mathbf{E})_\xi^I = \frac{D^I - (\mathbf{n}\cdot\mathbf{P})_\xi}{\epsilon_{0,\xi}}, \qquad \xi = L, R,$$

where D^I is defined by (49).

5. Stability and accuracy of the ADE-GDM interface approximations

In this section, the stability and accuracy of the ADE-GDM time-stepping schemes for model problems with and without interfaces are analyzed. We consider a one-dimensional model problem with an arbitrary number of polarization states and first show the stability of solutions for the continuous case. We then consider a second-order accurate semi-discretization in which spatial derivatives are discrete, while the time dependence remains continuous, and show stability for this case. Finally, the implications of the results for the fully discrete system for both second and fourth-order accuracy are investigated using a matrix stability approach in which the spectrum of the update operator is computed directly.

We recall that the stability[6] of the ADE-GDM scheme for a material with a single polarization state, and without interfaces, was considered previously in [12]. There it was shown that the second and fourth-order accurate schemes, with time step Δt and grid spacing h_l in each coordinate direction, are stable under the time-step restriction

$$\Delta t < \frac{C_{\text{cfl}}}{\sqrt{c^2\sum_{l=1}^d h_l^{-2}}}, \tag{51}$$

where $C_{\text{cfl}} = 1 - \mathcal{O}(\Delta t^2)$, provided that a sufficient condition on the GDM parameters for stability of the continuous problem is satisfied, namely $a_0 \geqslant 0$, $a_1 \geqslant 0$, $b_0 \geqslant 0$, $b_1 \geqslant 0$, and $a_0b_1 - a_1b_0 \geqslant 0$. Thus, the stability analysis presented here generalizes the previous results to multiple polarization states and to problems with interfaces.

5.1. Stability for a GDM material with multiple polarization states

We consider the following model problem in one space dimension for one component of the electric field coupled to multiple polarization states

$$\partial_t^2 E = c^2\partial_x^2 E - \epsilon_0^{-1}\partial_t^2 P, \qquad P \overset{\text{def}}{=} \sum_{m=1}^{N_p} P_m, \tag{52a}$$

---

[6] Here we use the term stability to indicate a lack of exponential growth in time. In particular, even *bounded* exponential growth at a fixed final time is forbidden.

$$\partial_t^2 P_m = \epsilon_0(a_{1,m}\partial_t E + a_{0,m}E) - b_{1,m}\partial_t P_m - b_{0,m}P_m, \tag{52b}$$

where $E(x,t)$ and $P_m(x,t)$ are scalar functions. For the pure initial-value problem (IVP) on the infinite domain $-\infty < x < \infty$ (Cauchy problem), or the IVP for a periodic problem on a finite domain, the model in (52) admits separable *plane-wave* solutions of the form $E = Ae^{st}e^{ikx}$, with $P_m = B_m e^{st}e^{ikx}$, if the real-valued wave number k and the dual Laplace-transform variable s satisfy the dispersion relation

$$s^2\big(1+\chi(s)\big) = -c^2k^2, \tag{53}$$

where the susceptibility χ is given by

$$\chi(s) = \sum_{m=1}^{N_p} \chi_m(s) = \sum_{m=1}^{N_p} \frac{a_{0,m} + a_{1,m}s}{b_{0,m} + b_{1,m}s + s^2}. \tag{54}$$

For the periodic problem, k must also be chosen so that the solution has the appropriate periodicity. For our purposes here we define stability (a stronger condition than well posedness) of the continuous Cauchy problem or periodic IVP as follows:

Definition 1. *The initial-value problem for* (52) *is said to be stable provided there are no solutions of the dispersion relation* (53) *with* $\mathrm{Re}(s) > 0$*.*

We note that this definition prohibits exponential growth in time, but does allow algebraic growth in time if there are multiple roots of the dispersion relation with $\mathrm{Re}(s) = 0$.

We now derive conditions on $\chi(s)$ so that there are no plane-wave solutions that have exponential grow in time. We note that these conditions, given below in Assumptions 1 and 2, and Theorem 1, do not depend on the particular form for $\chi(s)$ given by (54), and thus are applicable to a more general class of susceptibility functions.

Let s be a solution to the dispersion relation in (53). Let s and χ be written in terms of their real and imaginary parts as

$$s = s_r + is_i,$$
$$\chi = \chi_r + i\chi_i,$$

where there should be no confusion between χ_r and χ_i with the component susceptibilities χ_m, and it should be remembered that χ is a function of s. With these definitions, the real and imaginary parts of (53) yield the two real equations

$$(s_r^2 - s_i^2)(1+\chi_r) - 2s_r s_i \chi_i = -c^2k^2, \tag{55a}$$
$$(s_r^2 - s_i^2)\chi_i + 2s_r s_i(1+\chi_r) = 0. \tag{55b}$$

Before presenting a fundamental result regarding the stability of plane-wave solutions to the initial value problem for (52), we consider some special cases. The first special case is when $k = 0$. This is the constant mode in space, and the system in (52) reduces to ODEs. From (53) we must have $s^2 = 0$ or $\chi(s) = -1$. In the former case, there is a double root at $s = 0$, at least, which means there can be algebraic growth in time like t (or worse if $s = 0$ is also root of $1 + \chi$). This linear growth in time is a standard disease of the wave equation and is usually not a problem in practice if one is aware of the issue. More seriously there could be roots of $\chi(s)+1=0$ that lead to algebraic or exponential growth, and these we restrict by the following assumption.

Assumption 1. *We assume all roots to* $\chi(s)+1=0$ *satisfy* $\mathrm{Re}(s) \leqslant 0$*, and there are no roots at* $s=0$*.*

Note that the conditions in Assumption 1 can be determined by Routh-Hurwitz theory.

The second special case is when $k \neq 0$ but $\chi_i = \mathrm{Im}(\chi) = 0$. In this situtation $1+\chi \in \mathbb{R}$, and from (55b) it follows that $s_r = 0$, $s_i = 0$ or $1+\chi_r(s) = 0$. The case, $1+\chi_r(s)=0$, is covered by Assumption 1 and need not be considered. If $s_r = \mathrm{Re}(s) = 0$, then the solution is bounded. If $s_i = 0$, then (55a) implies

$$s_r^2\left(1+\chi_r(s_r)\right) = -c^2k^2. \tag{56}$$

The real equation in (56) has real solutions with $s_r > 0$ only if $1+\chi_r < 0$.

Assumption 2. *When* $k \neq 0$ *and* $\chi_i = 0$*, there are no real roots to equation* (56) *with* $s_r > 0$ *and* $1+\chi_r < 0$*.*

Having dealt with the two special cases, we are now ready to state our key result.

Theorem 1. *Plane-wave solutions of* (52) *with wave number* k *and Laplace variable* s *satisfying the dispersion relation* (53)*, as well as the conditions* $\mathrm{Im}(\chi) \neq 0$ *and* $k \neq 0$*, satisfy the condition*

$$\mathrm{Re}(s)\,\mathrm{Im}(s)\,\mathrm{Im}(\chi) > 0.$$

Thus, solutions decay exponentially in time (i.e. have $\mathrm{Re}(s) < 0$*), if*

$$\mathrm{Im}(s)\,\mathrm{Im}(\chi) < 0,$$

and grow exponentially in time (i.e. have $\mathrm{Re}(s) > 0$*), if*

$$\mathrm{Im}(s)\,\mathrm{Im}(\chi) > 0.$$

Proof. Dividing (55b) by $\chi_i \neq 0$ gives

$$s_r^2 - s_i^2 = -\frac{2s_r s_i}{\chi_i}(1+\chi_r),$$

and substituting this expression for $s_r^2 - s_i^2$ into (55a) leads to

$$2s_r\, s_i\, \chi_i \left[(1+\chi_r)^2 + \chi_i^2\right] = \chi_i^2\, c^2 k^2. \tag{57}$$

Since $\chi_i \neq 0$, $c \neq 0$ and $k \neq 0$, (57) implies $s_r \neq 0$ and $s_i \neq 0$. We thus have the main result that

$$s_r\, s_i\, \chi_i > 0.$$

If $s_i\chi_i = \mathrm{Im}(s)\,\mathrm{Im}(\chi) < 0$, then $s_r = \mathrm{Re}(s) < 0$ and solutions are decay exponentially. If, on the other hand, $s_i\chi_i > 0$, then $s_r > 0$ and solutions are grow exponentially. This completes the proof. □

We now provide sufficient conditions on the coefficients $a_{0,m}$, $a_{1,m}$, $b_{0,m}$ and $b_{1,m}$ of the component susceptibilties, χ_m, $m = 1, 2, \ldots, N_p$, in (54) so that there are no solutions that grow in time for $k \neq 0$. For $k = 0$, we still need Assumption 1, but we conjecture that the conditions in (58) below are sufficient to prevent roots with $\mathrm{Re}(s) > 0$ when $k = 0$.

Theorem 2. *If the coefficients of the GDM model satisfy*

$$a_{0,m} \geqslant 0, \quad a_{1,m} \geqslant 0, \quad b_{0,m} \geqslant 0, \quad b_{1,m} \geqslant 0, \tag{58a}$$

$$a_{0,m} b_{1,m} - a_{1,m} b_{0,m} \geqslant 0, \tag{58b}$$

for $m = 1, \ldots, N_p$, and if $\epsilon_0 > 0$ and $k \neq 0$, then plane-wave solutions of the GDM model in (52) with susceptibility given in (54) do not grow in time.

Proof. In addition to the conditions in (58a) we may assume that $a_{0,m} > 0$ or $a_{1,m} > 0$, otherwise $\chi_m = 0$ and this is an uninteresting case since P_m is uncoupled from E. We also note that if $N_p = 1$, then Assumption 1 holds. Now addressing Assumption 2, if the conditions in (58a) hold and if $a_{0,m} > 0$ or $a_{1,m} > 0$, then $s = s_r > 0$ implies $1 + \chi(s_r) > 0$ since

$$\chi = \sum_{m=1}^{N_p} \chi_m = \sum_{m=1}^{N_p} \frac{a_{0,m} + a_{1,m} s_r}{b_{0,m} + b_{1,m} s_r + s_r^2} > 0,$$

and thus Assumption 2 holds. We thus assume $\chi_i \neq 0$.

The imaginary part of χ_m is given by

$$\mathrm{Im}(\chi_m) = -\frac{\big[a_{1,m}|s|^2 + (a_{0,m} b_{1,m} - a_{1,m} b_{0,m})\big] s_i + 2 a_{0,m} s_r s_i}{d_m}, \tag{59}$$

where

$$d_m = \big| \, b_{0,m} + b_{1,m} s + s^2 \, \big|^2 \geqslant 0.$$

We note that if $b_{0,m} \geqslant 0$ and $b_{1,m} \geqslant 0$, then there are no solutions to $d_m = 0$ with $\mathrm{Re}(s) > 0$. From (57) it follows that

$$s_r \, s_i = \chi_i \frac{c^2 k^2}{2|1+\chi|^2} = \frac{\alpha^2}{2} \chi_i, \qquad \alpha \overset{\text{def}}{=} \frac{|ck|}{|1+\chi|} > 0. \tag{60}$$

Note that since $\chi_i \neq 0$ and $k \neq 0$ by assumption, (60) implies $s_r \neq 0$ and $s_i \neq 0$. Using (60) to replace $s_r s_i$ in (59) and summing over m gives

$$\chi_i = \sum_{m=1}^{N_p} \mathrm{Im}(\chi_m) = -s_i \sum_{m=1}^{N_p} \frac{a_{1,m}|s|^2 + (a_{0,m} b_{1,m} - a_{1,m} b_{0,m})}{d_m} - \chi_i \, \alpha^2 \sum_{m=1}^{N_p} \frac{a_{0,m}}{d_m}, \tag{61}$$

and solving for χ_i implies

$$\chi_i = -s_i \left[\sum_{m=1}^{N_p} \frac{a_{1,m}|s|^2 + (a_{0,m} b_{1,m} - a_{1,m} b_{0,m})}{d_m} \right] \left[1 + \alpha^2 \sum_{m=1}^{N_p} \frac{a_{0,m}}{d_m} \right]^{-1}. \tag{62}$$

In view of the conditions on $a_{0,m}$, $a_{1,m}$, $b_{0,m}$ and $b_{1,m}$ in (58) together with $a_{0,m} > 0$ or $a_{1,m} > 0$, the form of χ_i in (62) implies

$$\chi_i = -s_i\,\beta^2, \tag{63}$$

where $\beta^2 > 0$ is defined from (62), and therefore the product of the imaginary part of s times the imaginary part of χ is negative, i.e.

$$s_i\,\chi_i = -s_i^2\beta^2 < 0.$$

From Theorem 1 it follows that there are no solutions with $\mathrm{Re}(s) > 0$ that grow in time. This completes the proof. $\square$

We note that the conditions in (58) for $N_p = 1$ are the Routh-Hurwitz stability conditions corresponding to just one component susceptability, $\chi = \chi_1$. Thereom 2 then states that a sufficient condition for stability when $k \neq 0$ is that each individual χ_m satisfies the single-term Routh-Hurwitz stability conditions.

5.2. Stability of the continuous two-domain problem

Consider now the initial value problem for the continuous two-domain problem in one space dimension with $E_L(x,t)$ and $P_{L,m}(x,t)$ satisfying equations of the form in (52) with positive paramaeters $(c_L, \epsilon_{0,L}, \mu_{0,L})$ for $x < 0$, and $E_R(x,t)$, $P_{R,m}(x,t)$ satisfying similar equations with positive parameters $(c_R, \epsilon_{0,R}, \mu_{0,R})$ for $x > 0$. Note that the solution in each domain has N_{p_ξ} polarization states, $\xi = L$, R, defined by the GDM coefficients $a_{\xi,0,m}$, $a_{\xi,1,m}$, $b_{\xi,0,m}$ and $b_{\xi,1,m}$. (Throughout this section, the symbol ξ indicates L or R.) For this two-domain model problem, solutions satisfy the jump conditions

$$E_L(0,t) = E_R(0,t), \tag{64a}$$

$$\frac{1}{\mu_{0,L}}\partial_x E_L(0,t) = \frac{1}{\mu_{0,R}}\partial_x E_R(0,t), \tag{64b}$$

and they are assumed to be bounded as $x \to \pm\infty$. Recall that the Cauchy problem for each material separately is stable provided there are no solutions to the dispersion relation

$$s^2\big(1 + \chi_\xi(s)\big) = -c_\xi^2 k^2, \tag{65}$$

with $\mathrm{Re}(s) > 0$ and $k \in \mathbb{R}$. The next thereom states that the coupled problem is stable provided each material is stable in isolation.

Theorem 3. *If the Cauchy problem for each material separately is stable, then solutions to the two-domain problem with interface conditions* (64) *are also stable, i.e. there are no solutions with* $\mathrm{Re}(s) > 0$.

Proof. The proof proceeds by showing there are no unstable solutions with $\mathrm{Re}(s) > 0$ of the form

$$E_\xi(x,t) = e^{st}\hat{E}_\xi(x), \qquad P_{\xi,m}(x,t) = e^{st}\hat{P}_{\xi,m}(x). \tag{66}$$

Note that in order to satisfy the interface conditions, it is necessary that the time factors are the same for the solutions in the left and right domains, i.e. s has the same value for $\xi = L$ and R. An implication of this is that solutions on the left and right are either both stable or unstable. Substituting (66) into the governing equations and interface/boundary conditions, and eliminating $\widehat{P}_{\xi,m}(x)$, we find that $\widehat{E}_\xi(x)$ solves the ODEs

$$c_\xi^2 \widehat{E}_\xi'' - s^2\big(1 + \chi_\xi(s)\big)\widehat{E}_\xi = 0, \qquad \xi = L,\, R, \tag{67}$$

subject to the interface conditions

$$\widehat{E}_L(0) = \widehat{E}_R(0), \tag{68a}$$

$$\frac{1}{\mu_{0,L}}\widehat{E}_L'(0) = \frac{1}{\mu_{0,R}}\widehat{E}_R'(0), \tag{68b}$$

and the requirement that solutions are bounded as $x \to \pm\infty$. General solutions of (67) have the form

$$\widehat{E}_\xi(x) = A_\xi e^{\lambda_\xi x} + B_\xi e^{-\lambda_\xi x}, \tag{69}$$

where A_ξ and B_ξ are constants, and λ_ξ is a function of s satisfying

$$c_\xi^2 \lambda_\xi^2 - s^2(1 + \chi_\xi(s)) = 0, \qquad \xi = L,\, R. \tag{70}$$

We now look for unstable solutions with $\mathrm{Re}(s) > 0$. We first rule out the case $\mathrm{Re}(\lambda_\xi) = 0$. If $\mathrm{Re}(\lambda_\xi) = 0$ for $\xi = L$ or R so that $\lambda_\xi = ik_\xi$, then (70) takes the form

$$s^2(1 + \chi_\xi(s)) = -c_\xi^2 k_\xi^2, \tag{71}$$

for some $k_\xi \in \mathbb{R}$, which has the same form as (65). Since the Cauchy problem is stable by assumption, the roots of (71) must have $\mathrm{Re}(s) \leqslant 0$. Therefore, any unstable solutions with $\mathrm{Re}(s) > 0$ cannot have $\mathrm{Re}(\lambda_\xi) = 0$ in either domain (since both sides have the same value for s).

It remains to check stability for the case when $\mathrm{Re}(\lambda_L) \neq 0$ and $\mathrm{Re}(\lambda_R) \neq 0$. Suppose $\mathrm{Re}(\lambda_L) > 0$ and $\mathrm{Re}(\lambda_R) > 0$ without loss of generality, so that bounded solutions are

$$\begin{aligned} \widehat{E}_L(x) &= A_L e^{\lambda_L x}, \quad && x \leqslant 0, \\ \widehat{E}_R(x) &= B_R e^{-\lambda_R x}, \quad && x \geqslant 0. \end{aligned}$$

The interface conditions in (68) yield the two linear equations

$$\begin{aligned} A_L &= B_R, \\ A_L\left(\frac{\lambda_L}{\mu_{0,L}}\right) &= -B_R\left(\frac{\lambda_R}{\mu_{0,R}}\right). \end{aligned}$$

Nontrivial solutions of these equations imply

$$\frac{\lambda_L}{\mu_{0,L}} = -\frac{\lambda_R}{\mu_{0,R}}. \tag{72}$$

There are, however, no solutions to (72) when $\mathrm{Re}(\lambda_\xi) > 0$, since the real part of the left-hand side is positive while the real part of the right-hand side is negative. Thus, we have shown that there are no solutions to the two-domain problem with $\mathrm{Re}(s) > 0$, and this completes the proof. $\square$

5.3. Stability of the semidiscrete model problem

We now discretize the model problem in (52) using a second-order accurate approximation in space while keeping time continuous,

$$\partial_t^2 E_{\xi,j} = c_\xi^2\, D_{+x} D_{-x} E_{\xi,j} - \epsilon_{0,\xi} \sum_{m=1}^{N_{p,\xi}} \partial_t^2 P_{\xi,m,j}, \tag{73a}$$

$$\left(\partial_t^2 + b_{\xi,1,m}\partial_t + b_{\xi,0,m}\right) P_{\xi,m,j} = \epsilon_{0,\xi}\left(a_{\xi,1,m}\partial_t + a_{\xi,0,m}\right) E_{\xi,j}, \tag{73b}$$

for $\xi = L, R$. Here, D_{+x} and D_{-x} are, respectively, forward and backward divided difference operators in the x direction with grid spacing h_ξ. For the infinite-domain initial-value problem (Cauchy problem) the eigen-solutions of (73) have the same form as those for the continuous case, e.g., $E_{\xi,j} = Ae^{st}e^{ik_\xi x_j}$, $x_j = jh_\xi$, where $s \in \mathbb{C}$ and $k_\xi \in \mathbb{R}$ now satisfy

$$s^2\left(1 + \chi_\xi(s)\right) = -c^2\,\frac{4\sin^2(k_\xi h_\xi/2)}{h_\xi^2}, \tag{74}$$

noting that

$$D_{+x}D_{-x}e^{ik_\xi x_j} = -\frac{4\sin^2(k_\xi h_\xi/2)}{h_\xi^2}\, e^{ik_\xi x_j}.$$

Equation (74) is a discrete analog of the continuous dispersion relation in (53). As in the continuous case, the Cauchy problem is stable provided there are no roots to (74) with $\mathrm{Re}(s) > 0$. Since $\sin^2(k_\xi h_\xi/2) \geqslant 0$ we note that the discrete Cauchy problem is stable provided the corresponding continuous problem is stable.

The two-domain problem is now discretized using (73) as follows:

$$\partial_t^2 E_{L,j} = c_L^2\, D_{+x} D_{-x} E_{L,j} - \epsilon_{0,L}^{-1} \sum_{m=1}^{N_{p,L}} \partial_t^2 P_{L,m,j}, \qquad j = \ldots, -2, -1, 0, \tag{75a}$$

$$\left(\partial_t^2 + b_{L,1,m}\partial_t + b_{L,0,m}\right) P_{L,m,j} = \epsilon_{0,L}\left(a_{L,1,m}\partial_t + a_{L,0,m}\right) E_{L,j}, \qquad j = \ldots, -2, -1, 0, \tag{75b}$$

$$\partial_t^2 E_{R,j} = c_R^2\, D_{+x} D_{-x} E_{R,j} - \epsilon_{0,R}^{-1} \sum_{m=1}^{N_{p,R}} \partial_t^2 P_{R,m,j}, \qquad j = 0, 1, 2, 3, \ldots, \tag{75c}$$

$$\left(\partial_t^2 + b_{R,1,m}\partial_t + b_{R,0,m}\right) P_{R,m,j} = \epsilon_{0,R}\left(a_{R,1,m}\partial_t + a_{R,0,m}\right) E_{R,j}, \qquad j = 0, 1, 2, 3, \ldots, \tag{75d}$$

Here, we note that ghost points are introduced on either side of the interface at $j = 0$ ($x = 0$), and the interface conditions are used determine their values. Following the discussion in Section 4.1, the governing equation in (52a) is used with the interface condition in (64a) to generate a compatibility condition involving the second derivative of E_ξ with respect to x (as well as time derivatives of

$P_{\xi,m}$), which is then discretized in space. This leads to the discrete interface conditions

$$\begin{aligned} c_L^2 D_{+x} D_{-x} E_{L,0} - \epsilon_{0,L}^{-1} \sum_{m=1}^{N_{p,L}} \partial_t^2 P_{L,m,0} &= c_R^2 D_{+x} D_{-x} E_{R,0} - \epsilon_{0,R}^{-1} \sum_{m=1}^{N_{p.R}} \partial_t^2 P_{R,m,0}, && (76a) \\ \mu_{0,L}^{-1} D_{0x} E_{L,0} &= \mu_{0,R}^{-1} D_{0x} E_{0,R}, && (76b) \end{aligned}$$

where D_{0x} is the centered divided difference operator in the x direction. We also impose conditions that the solutions remain bounded as $j \to \pm\infty$,

$$\begin{aligned} |E_{L,j}| &\leqslant C_L, \qquad j \to -\infty, && (77a) \\ |E_{R,j}| &\leqslant C_R, \qquad j \to +\infty, && (77b) \end{aligned}$$

where C_L and C_R are constants. These equations are augmented with appropriate initial conditions. Stability of this discrete approximation is encapsulated in the following theorem.

Theorem 4. *The initial boundary-value problem for the discretization* (75)*, with interface conditions* (76) *and boundary conditions* (77)*, does not admit exponentially growing solutions provided the Cauchy problem for each semi-discretization in isolation has no growing modes and the parameters in the GDM model satisfy conditions* (58)*.*

Proof. As before, we consider separable solutions of the form

$$E_{\xi,j}(t) = e^{st} \widehat{E}_{\xi,j}, \qquad P_{\xi,m,j}(t) = e^{st} \widehat{P}_{\xi,m,j}, \tag{78}$$

and show that no solutions exist with $\operatorname{Re}(s) > 0$. Substituting the forms in (78) into the discrete equations in (75) and (76), and eliminating $\widehat{P}_{\xi,m,j}$, gives

$$\begin{aligned} c_L^2 D_{+x} D_{-x} \widehat{E}_{L,j} - s^2 \big(1 + \chi_L(s)\big) \widehat{E}_{L,j} &= 0, \qquad j = \dots, -2, -1, 0, && (79a) \\ c_R^2 D_{+x} D_{-x} \widehat{E}_{R,j} - s^2 \big(1 + \chi_R(s)\big) \widehat{E}_{R,j} &= 0, \qquad j = 0, 1, 2, 3, \dots, && (79b) \end{aligned}$$

with interface conditions

$$\begin{aligned} c_L^2 D_{+x} D_{-x} \widehat{E}_{L,0} - s^2 \chi_L(s) \widehat{E}_{L,0} &= c_R^2 D_{+x} D_{-x} \widehat{E}_{R,0} - s^2 \chi_R(s) \widehat{E}_{R,0}, && (80a) \\ \mu_{0,L}^{-1} D_{0x} \widehat{E}_{L,0} &= \mu_{0,R}^{-1} D_{0x} \widehat{E}_{R,0}. && (80b) \end{aligned}$$

General solutions of the difference equations in (79) have the form

$$\widehat{E}_{\xi,j} = A_\xi \kappa_{\xi,+}^j + B_\xi \kappa_{\xi,-}^j, \tag{81}$$

where A_ξ and B_ξ are constants, and $\kappa_{\xi,\pm}$ are roots of the characteristic polynomial

$$\kappa^2 - 2\left(1 + \frac{1}{2} z_\xi\right) \kappa + 1 = 0. \tag{82}$$

The parameter z_ξ in (82) is given by

$$z_\xi \overset{\text{def}}{=} \lambda_\xi^2 h_\xi^2 = \frac{h_\xi^2}{c_\xi^2}\, s^2(1+\chi_\xi(s)), \tag{83}$$

where λ_ξ, defined previously in (70), depends on s.

As in the continuous two-domain model problem, we can use (83), (74), and stability of the Cauchy problems to rule out the case when $\operatorname{Re}(\lambda_L) = 0$ or $\operatorname{Re}(\lambda_R) = 0$, and focus the analysis on the case when $\operatorname{Re}(\lambda_\xi) \neq 0$. For this latter case, roots of (82) can be defined such that one root has magnitude greater than one, while the other has magnitude less than one. (Note that the product of the roots is one.) This property is helpful to identify solutions in (81) that decay or grow as $j \to \pm\infty$. For this purpose, it is convenient to express the roots of (82) in the form

$$\kappa_{\xi,\pm} = 1 + \frac{1}{2} z_\xi \pm \sqrt{z_\xi}\,\sqrt{1+\frac{1}{4} z_\xi}\,, \tag{84}$$

where the principal branch of the square root functions are assumed. Figure 4 shows the behavior of $|\kappa_{\xi,\pm}|$ as a function of the real and imaginary parts of z_ξ. We observe that $|\kappa_{\xi,\pm}| = 1$ if and only if z_ξ is real and $-4 \leqslant z_\xi \leqslant 0$. Note that z_ξ defined in (83) cannot be real with $z_\xi \leqslant 0$ since $\operatorname{Re}(\lambda_\xi) \neq 0$. Thus, $|\kappa_{\xi,+}| > 1$ and $|\kappa_{\xi,-}| < 1$, and bounded solutions of the difference equations in the left and right domains from (81) are

$$\widehat{E}_{L,j} = A_L \kappa_{L,+}^j, \qquad \widehat{E}_{R,j} = B_R \kappa_{R,-}^j. \tag{85}$$

The discrete interface condition in (80a), together with the difference equations in (79) at $j = 0$, imply

$$s^2 \widehat{E}_{L,0} = s^2 \widehat{E}_{R,0},$$

and thus $A_L = B_R$ as in the continuous problem. Note that we have assumed implicitly that the initial conditions for E_ξ and $\partial_t E_\xi$ satisfy the primary jump condition $E_L(0,t) = E_R(0,t)$. The second interface condition in (80b) then requires

$$\mu_{0,L}^{-1}\left(\frac{\kappa_{L,+} - \kappa_{L,+}^{-1}}{2h_L}\right) = -\mu_{0,R}^{-1}\left(\frac{\kappa_{R,-} - \kappa_{R,-}^{-1}}{2h_R}\right),$$

for nontrivial solutions to exist. Substituting for $\kappa_{L,+}$ and $\kappa_{R,-}$, and using $\kappa_{\xi,+}\kappa_{\xi,-} = 1$, gives

$$\frac{\sqrt{z_L}\,\sqrt{1+z_L/4}}{\mu_{0,L}\, h_L} = -\frac{\sqrt{z_R}\,\sqrt{1+z_R/4}}{\mu_{0,R}\, h_R}. \tag{86}$$

The condition in (86) is a discrete analog of (72), and if it can be shown that there are no solutions of (86) with $\operatorname{Re}(s) > 0$, then the proof is complete. For the discrete case, this last step of the proof involves technical details involving bounds on the terms in (86), which make use of the conditions in (58) on the GDM parameters. These details are provided in Appendix A to complete the proof.

□

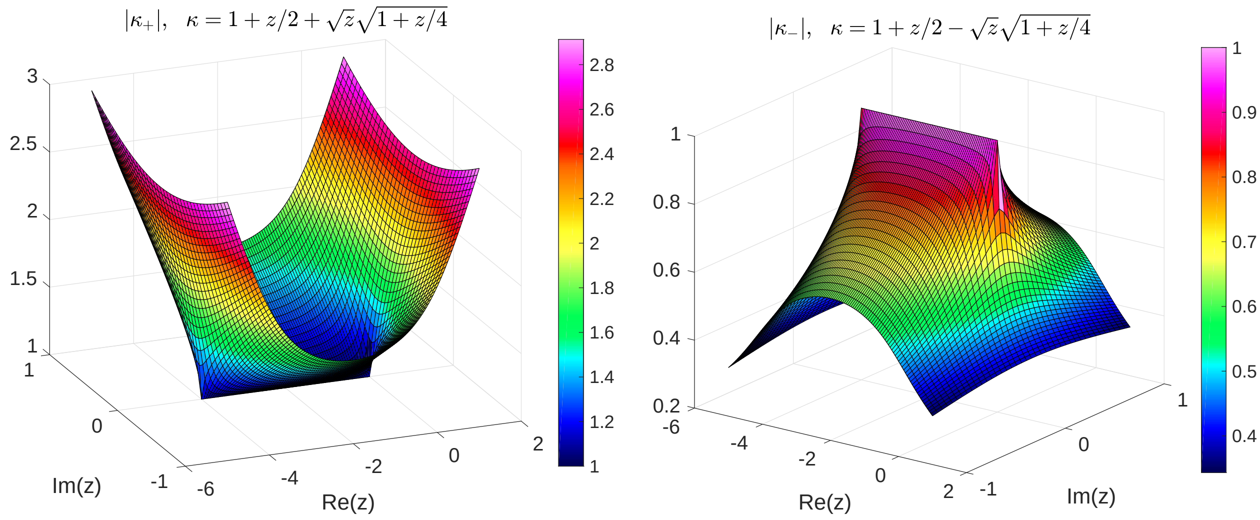

Figure 4: Surface plots of $|\kappa_+|$ and $|\kappa_-|$ versus z, $\kappa_\pm = 1 + z/2 \pm \sqrt{z}\sqrt{1+z/4}$.

5.4. Matrix stability analysis of the ADE-GDM schemes

To further investigate the properties of the interface approximations, a matrix stability analysis is performed for fully discrete second-order and fourth-order accurate approximations of the system in (52) for a two-domain problem. In this approach, the eigenvalues of the time-stepping matrix are checked to determine whether the schemes admit growing solutions in time. It is shown numerically that the time-stepping schemes with ADE-GDM interface conditions are stable over a range of GDM parameters provided these parameters are chosen to satisfy the Routh-Hurwitz stability conditions in each domain as in (58).

We consider the solution to a two-domain problem in one space dimension using fully discrete ADE-GDM space-time schemes. The second-order accurate version of the scheme takes the form

$$D_{+t}D_{-t}E_j^n = c^2 D_{+x}D_{-x}E_j^n - \epsilon_0^{-1} D_{+t}D_{-t}P_j^n, \tag{87a}$$

$$D_{+t}D_{-t}P_j^n + b_1 D_{0t}P_j^n + b_0 P_j^n = a_0 E_j^n + a_1 D_{0t}E_j^n, \tag{87b}$$

for a range of j on each material domain, and assuming a single polarization state. Here, E_j^n corresponds to a tangential component of the field to be consistent with the interface conditions given below. We use two material domains, denoted by left and right. Dirichlet boundary conditions are imposed on the far left and far right boundaries. At the interface between the two material domains the discrete interface conditions take the form

$$\left[\mu_0^{-1} D_{0x}E_j^n\right]_I = 0, \tag{88a}$$

$$\left[(c^2 - \epsilon_0^{-1}K) D_{+x}D_{-x}E_j^n + c_0 E_j^n + c_1 E_j^{n-1} + d_0 P_j^n + d_1 P_j^{n-1}\right]_I = 0, \tag{88b}$$

for constants K, $\{c_0, c_1\}$ and $\{d_0, d_1\}$, whose values can be determined following the approach described in Section 4.1 and summarized in (27) and (28) for the second-order case.

We first verify the accuracy of the second-order accurate scheme in (87) and (88), and the corresponding fourth-order scheme, by performing a grid refinement study. The left and right domains are taken to be $x \in [-\pi, 0]$ and $x \in [0, \pi]$, respectively, with $x = 0$ being the position of the interface. The material parameters for each domain are

Material	ϵ_0	N_p	a_0	a_1	b_0	b_1
left	1	1	2	0.6	0.4	0.9
right	4	1	1.1	0.7	0.8	1.2

with $\mu_0 = 1$ on both sides. An exact solution can found to the scattering problem with incident field

$$E^{(i)}(x,t) = e^{-i\omega t}e^{ikx},$$

where $\omega = 5$ and the wave number $k \in \mathbb{C}$ chosen to satisfy the dispersion relation in the left domain. The initial conditions and boundary conditions for the numerical schemes are taken from the exact solution.

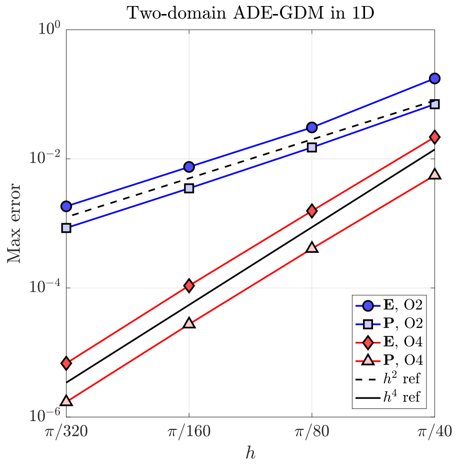

Figure 5: Maximum errors versus grid spacing for the one-dimensional ADE-GDM test code for interfaces. The legend indicates “O2” for the second-order scheme and “O4” for the fourth-order scheme.

Figure 5 shows the max-norm errors of the solutions of the second-order and fourth-order accurate schemes versus grid spacing for the one-dimensional two-domain problem. The time step for each grid with mesh spacing h is chosen to satisfy the CFL condition

$$\max_{\xi=L,R}\{c_\xi\}\,\frac{\Delta t}{h} = C_{\text{cfl}},$$

where $c_\xi = 1/\sqrt{\epsilon_{0,\xi}\mu_{0,\xi}}$, $\xi = L, R$, are the wave speeds in the left and right domains, and $C_{\text{cfl}} = 0.9$. The errors shown in the figure indicate that the fully discrete time-stepping schemes with interface approximations are converging at their expected rates.

Having verified the convergence of the schemes for one set of GDM parameters, we now consider their stability for a range of parameters. The second and fourth-order schemes are both three-level schemes in time, and can be written in matrix form as

$$\begin{bmatrix} \mathbf{q}^{n+1} \\ \mathbf{q}^{n} \end{bmatrix} = A \begin{bmatrix} \mathbf{q}^{n} \\ \mathbf{q}^{n-1} \end{bmatrix}, \qquad A \overset{\text{def}}{=} \begin{bmatrix} A_{11} & A_{12} \\ I & 0 \end{bmatrix}.$$

Here, $\mathbf{q}^n$ is a vector that holds the discrete values for E_j^n and P_j^n on both domains, and A is the time-stepping matrix. The scheme is stable, by which we mean no growth in time, if all eigenvalues λ of A have magnitude less than or equal to one, $|\lambda| \leqslant 1$, and there are no defective multiple eigenvalues with $|\lambda| = 1$. For example, for the non-dissipative case we expect all eigenvalues to satisfy $|\lambda| = 1$. More generally one could allow bounded exponential growth in time for which $|\lambda| \leqslant 1 + \mathcal{O}(\Delta t)$.

The entries in the time-stepping matrix are evaluated directly from the time-stepping code using a discrete delta-function approach, which is implemented as follows. Consider a generic linear system $A\mathbf{x} = \mathbf{b}$, with $A \in \mathbb{R}^{m\times m}$, $\mathbf{x} \in \mathbb{R}^m$ and $\mathbf{b} \in \mathbb{R}^m$, for which we only know how to compute the residual

$$\mathbf{r}(\mathbf{y}) = A\mathbf{y} - \mathbf{b}, \tag{89}$$

for a given vector $\mathbf{y} \in \mathbb{R}^m$. The entries in column i of A, denoted by $\mathbf{a}_i$, are then found by evaluating the residual using

$$\mathbf{a}_i = \mathbf{r}(\mathbf{e}_i) - \mathbf{r}(\mathbf{0}),$$

where $\mathbf{e}_i$ is the unit vector (*discrete delta function*) with a one at position "i" and zeros elsewhere. This approach is implemented easily, and it also helps to ensure that the time-stepping matrix agrees with the time-stepping code. We note that some care must be taken to deal with constraint equations, such as the interface and boundary conditions, since we have found it easiest to evaluate the eigenvalues if these constraint equations and their associated unknowns (e.g. ghost point values) have been eliminated.

Figure 6 shows matrix stability results for the second-order and fourth-order accurate schemes as a function of a_0 and b_0 on the left domain. The figures are created by computing the spectral radius

$$\rho(A) = \max |\lambda_i(A)|,$$

of the time-stepping matrix for different discrete values of the parameters a_0 and b_0 in the left domain. There are always some eigenvalues with modulus very near one, and thus the contours of $\rho(A)$ in the stable region are very close to one. The figures show that the scheme is stable in the region of parameter space where the Routh-Hurwitz condition $a_1 b_0 < a_0 b_1$, is satisfied. For comparsion, the stability regions were generated for two different grid spacings of $\Delta x = \pi/N$ with $N = 10$ and $N = 20$. The regions are very similiar for the two grid spacings.

6. Numerical results

This section presents results to verify the accuracy and stablility of the new interface conditions. The first test case considers scattering of a dispersive plane wave from a planar interface between two dispersive media. This simple geometry acts as a benchmark for more complex configurations. The second test case looks at scattering of a plane wave from a two-dimensional cylinder (disk) in which the regions interior and exterior to the disk are dispersive. Scattering from a dispersive sphere is evaluated as a third verification. A final more complex example shows scattering from a collection of dispersive objects to demonstrate the flexibility of the approach.

6.1. Scattering from a planar interface between two dispersive materials

This section considers the scattering of a plane wave from the flat interface between two dispersive materials; this is a simple but fundamental test of the new interface conditions. The incident

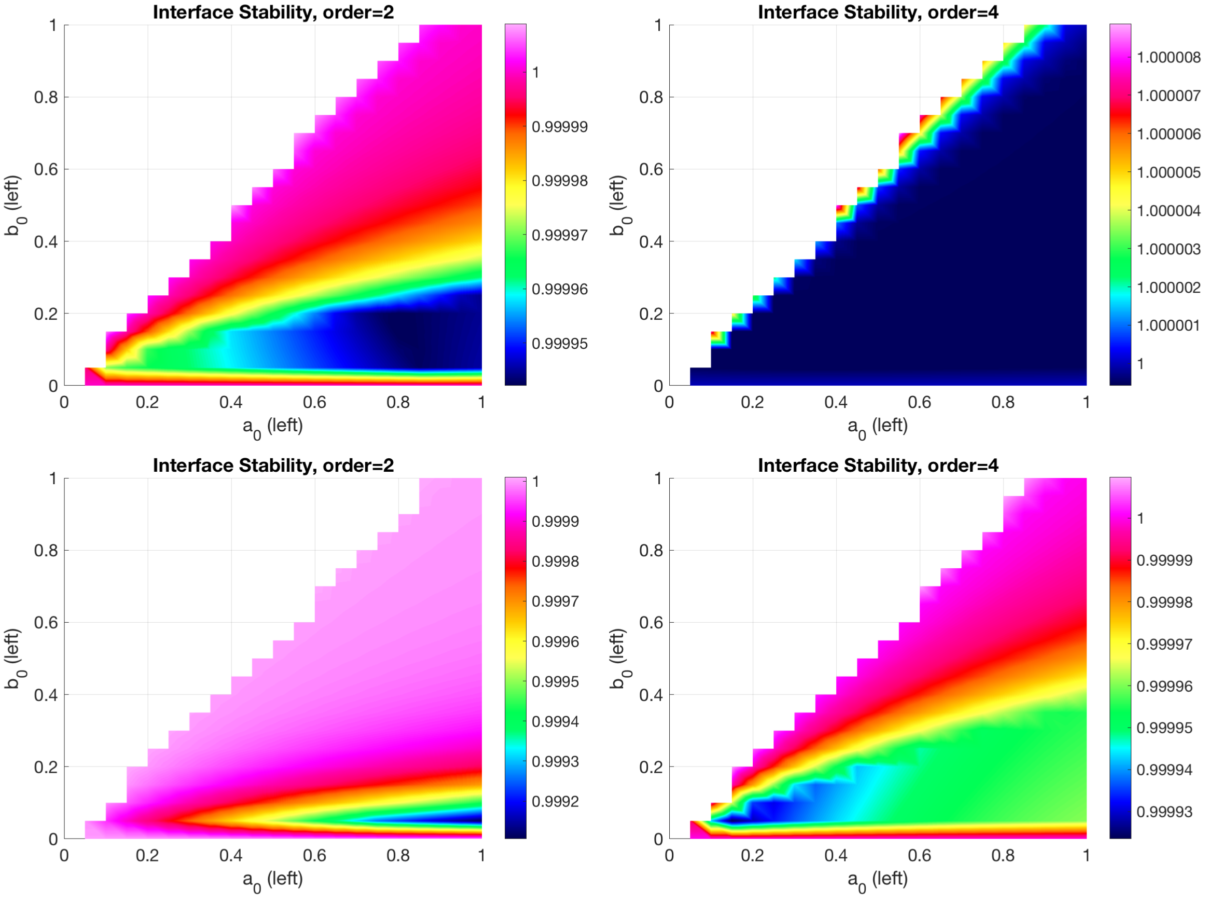

Figure 6: Matrix stability results for the second-order accurate interface scheme (left) and fourth-order accurate interface scheme (right). Regions of stability (no growth in time) varying a_0 and b_0 on the left side of the interface. Contours of the spectral radius, $\rho(A)$, are plotted (not shown when $\rho(A) > 1 + \epsilon$, where $\epsilon = 10^{-5}$). Top: $h = \pi/20$, bottom: $h = \pi/10$.

wave, originating in the *left* domain, is taken in the form of a plane wave,

$$\mathbf{E}^{(i)} = \mathbf{a}\, e^{st}\, e^{i\mathbf{k}\cdot\mathbf{x}}, \tag{90}$$

where $s \in \mathbb{C}$, $\mathbf{k}$ is the incident wave-number vector, and $\mathbf{a}$ is an amplitude vector satisfying $\mathbf{k}^T\mathbf{a} = 0$ (since $\nabla\cdot\mathbf{E}^{(i)} = 0$). The exact solution for dispersive materials has the same form as the well-known solution for non-dispersive materials [18]. The exact solution is defined in terms of a root s to the dispersion relation for the left domain which depends on $\mathbf{k}$ and the GDM parameters in the left domain. There are multiple roots to this dispersion relation, corresponding to multiple fundamental modes, and we choose either a *non-resonant* (NR) mode, which is a pertubation of a root to the non-dispersive equations (i.e. $s \approx -ic|\mathbf{k}|$), or a *resonant* (R) mode, which is a new dispersive root. See [12] for further details on resonant and non-resonant modes.

The second and fourth-order accurate time-stepping schemes described in Algorithms 1 and 2, respectively, are used to compute approximate solutions. The initial conditions and boundary conditions for the time-stepping schemes are assigned from the exact solution, and the second and fourth-order accurate interface conditions described in Section 4 are used to assign ghost points adjacent to the interface. The computational grids, denoted by $\mathcal{G}^{(\ell)}$, have a target grid spacing approximately equal to $\Delta s^{(\ell)} = 1/(10\ell)$. In two dimensions, the left domain is the square $[-1, 0] \times [0, 1]$, while the right domain is the adjacent square $[0, 1] \times [0, 1]$. In three dimensions, the left domain is the box $[-1, 0] \times [0, .5] \times [0, .5]$, while the right domain is the adjacent box $[0, 1] \times [0, .5] \times [0, .5]$. In three dimensions, the grid spacing in the x-direction (normal to the interface) is smaller by a factor of 0.75 to avoid the tall-cell interface issue as discussed in Section 4.3.

In two dimensions, we take GDM materials with three polarization vectors on the left and two on the right, and consider the case of an incident wave hitting the interface at an oblique angle. The relavent parameters are:

Material	ϵ_0	N_p	$a_{0,m}$	$a_{1,m}$	$b_{0,m}$	$b_{1,m}$
left	3	3	$[1, 1.5, 2]$	$[.1, .07, .05]$	$[1, 1.5, 2]$	$[.2, .1, .05]$
right	2	2	$[1.2, 1.4]$	$[.1, .15]$	$[.8, 1.2]$	$[.05, .09]$
NR-mode: $s \approx (-.113635, -10.1600)$						
R-mode: $s \approx (-.098328, -.989946)$						

with

$$\mathbf{k} = 2\pi \frac{[2, 1, 0]^T}{\sqrt{2^2 + 1^2}}, \qquad \mathbf{a} = \frac{[-1, 2, 0]^T}{\sqrt{1^2 + 2^2}}.$$

In three dimensions, we take GDM materials with two polarization vectors on the left and one on the right, and again consider an incident wave hitting the interface at an oblique angle. The relavent parameters are:

Material	ϵ_0	N_p	$a_{0,m}$	$a_{1,m}$	$b_{0,m}$	$b_{1,m}$
left	1	2	$[1, 1.5]$	$[.1, .125]$	$[1, 1.5]$	$[.2, .1]$
right	2	1	$[1]$	$[.1]$	$[1]$	$[.2]$
NR-mode: $s = (-.114013, -14.4821)$						
R-mode: $s = (-.0992613, -.9926566)$						

with

$$\mathbf{k} = 2\pi \frac{[2, 1, 0.5]^T}{\sqrt{2^2 + 1^2 + 0.5^2}}, \qquad \mathbf{a} = \frac{[-1, 2, 0]^T}{\sqrt{1^2 + 2^2}}.$$

Figure 7 shows contours on cutting planes for the solution component E_z and the error in E_z. Note that E_z has only scattered and transmitted field components. The solution and the error are seen to be smooth in each domain, which indicates there are no visible spurious effects caused by the discrete interface conditions.

Figure 8 shows graphs of the max-norm errors at time $t = 0.5$ as a function of grid-spacing for the second-order accurate scheme (blue lines) and fourth-order accurate scheme (red lines). Results are shown in two and three dimensions for a resonant (R) and non-resonant (NR) mode. Errors reported for a vector such as $\mathbf{E}$ denote the maximum error over all its components and over all grid points. The graphs clearly show that the numerical schemes are converging at very close to the expected rates for both $\mathbf{E}$ and $\mathbf{P}$. As expected the errors in the fourth-order accurate scheme become much smaller than those for the second-order accurate scheme as the mesh is refined.

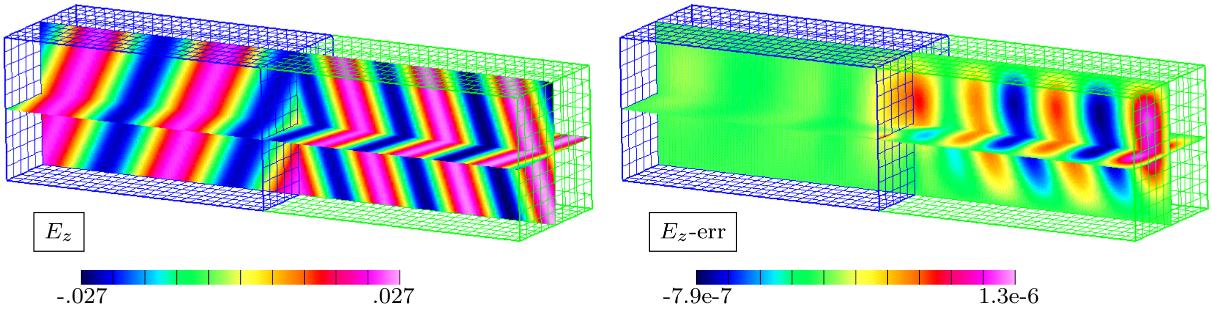

Figure 7: Scattering at a planar interface between two dispersive material in three dimensions. Contours of the solution component E_z (left) and the error in E_z (right) are shown on selected cutting planes at time $t = 0.5$. The solution was computed on grid $\mathcal{G}^{(8)}$ (coarsened grid lines on the boundary are shown).

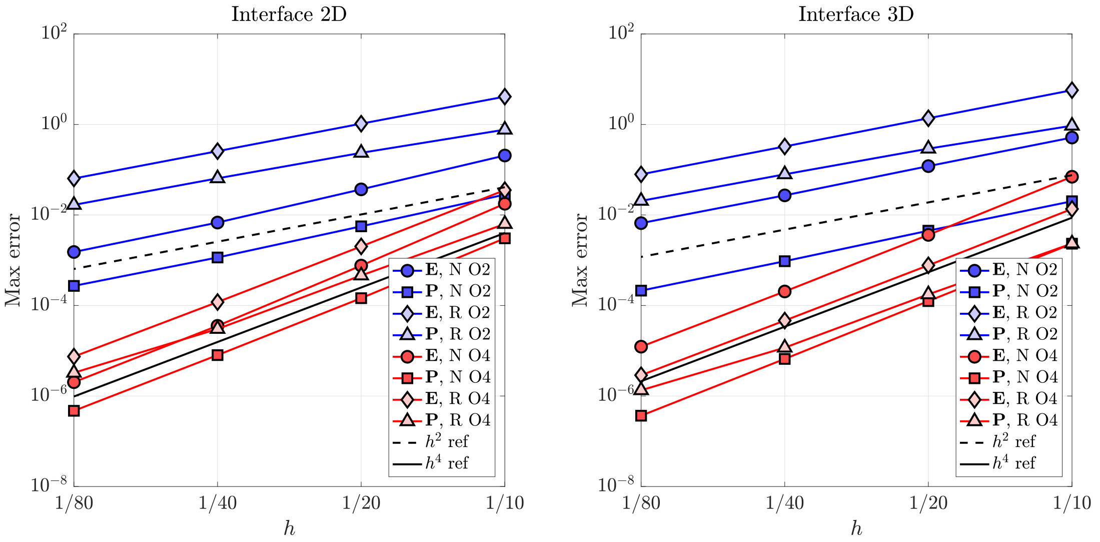

Figure 8: Maximum errors versus grid spacing for scattering of a dispersive plane wave from an planar interface. Left: two dimensions. Right: three dimensions. The legends indicate "O2" for the second-order scheme and "O4" for the fourth-order, while "N" denotes the non-resonant mode and "R" the resonant mode.

6.2. Scattering from a two-dimensional dispersive dielectric disk

Consider a two-dimensional circular disk of one dispersive material embedded in a second dispersive material. The solution to the scattering of a TE-z plane wave in the outer domain impinging on the disk can be determined as a Mie series in the same manner as for non-dispersive materials [24] except that the series involves Bessel functions with complex arguments. The incident electric field takes the form

$$H_z = a_z e^{st}\, e^{ikx}, \qquad E_y = -a_z \frac{ik}{s\hat{\epsilon}_o(s)}\, e^{st}\, e^{ikx},$$

where a_z defines the amplitude of the wave and $\hat{\epsilon}_o(s)$ is the permittivity in the outer domain. For a given wave number k, $s \in \mathbb{C}$ is chosen as a root of the dispersion relation in the outer domain. As noted in the previous section, there are multiple possible roots to the dispersion relation. When the outer domain is dispersive there are both resonant and non-resonant modes, and we show results and grid convergence for both types of fundamental modes.

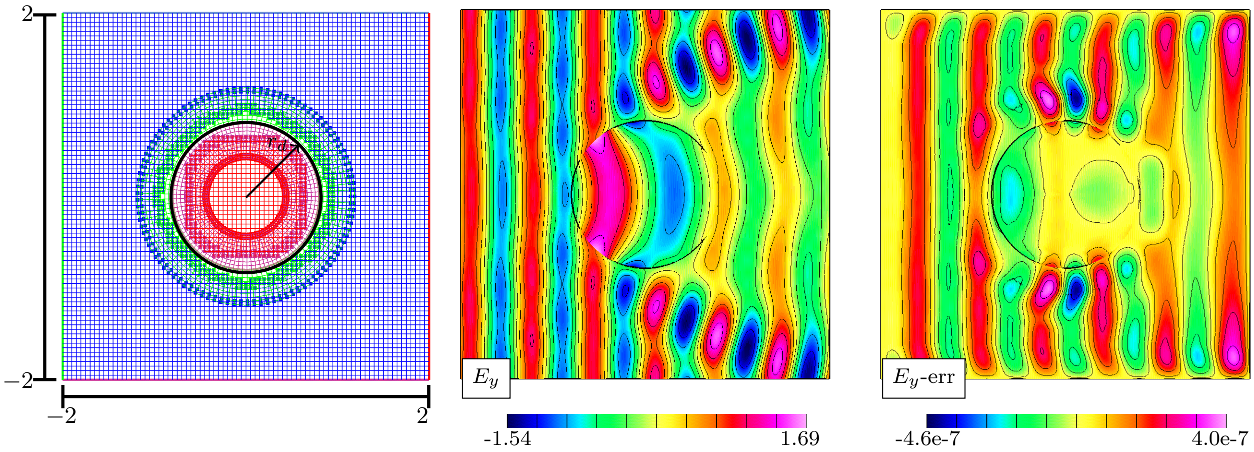

Figure 9: Left: A coarse grid representation of the composite grid $\mathcal{G}^{(2)}$ for the dielectric disk. Middle: The E_y field for the NR-mode on grid $\mathcal{G}^{(16)}$ at $t = 0.3$ computed using the fourth-order accurate ADE-GDM scheme. Right: The the error in the computed E_y field.

The geometry of the problem consists of a disk of radius $r_d = 0.4$ enclosed in a larger square domain with dimensions $[-2, 2] \times [-2, 2]$. The composite grid for the domain, of resolution factor ℓ, is denoted by $\mathcal{G}_d^{(\ell)}$ and has grid spacing approximately equal to $\Delta s^{(\ell)} = 1/(20\ell)$. The composite grid, as shown in the left plot of Figure 9, consists of four component grids. The region outside the disk is covered with a blue Cartesian grid and a green interface-fitted grid. The region inside the disk is covered with a red Cartesian grid and a pink interface-fitted grid. The region interior to the disk is covered by an annular interface-fitted grid and an interior Cartesian grid. The outer domain also consists of an annular interface-fitted grid and a background Cartesian grid.

The boundary conditions on the outer square are taken from the exact solution. The initial conditions are also assigned from the exact solution. The interface is treated using our new discrete conditions. The outer domain is taken as a dispersive material with one polarization vector, while the region inside the disk is a dispersive material with two polarization vectors. The exact solution is defined for $k = 3(2\pi)$ and $a_z = 1$, and the remaining parameters are given as follows:

Material	ϵ_0	N_p	$a_{0,m}$	$a_{1,m}$	$b_{0,m}$	$b_{1,m}$
outer	1	1	[1]	[0.1]	[1]	[0.2]
inner	0.25	2	$[1.2, 1.4]$	$[0.1, 0.15]$	$[0.8, 1.2]$	$[0.05, 0.09]$
NR-mode: $s = (-0.050417, -18.8755)$						
R-mode: $s = (-0.099583, -0.993642)$						

Figure 9 shows contours of the solution component E_y and the error in E_y. The solution and the error are seen to be quite smooth in each domain near the interface (the error can jump at the interface since the solution can also jump) which indicates there are no visible spurious effects caused by the discrete interface conditions. There is a small visible change in the contour lines of the error near the interpolation points (note that the contours are independently plotted twice in the overlap region), but this is not unusual.

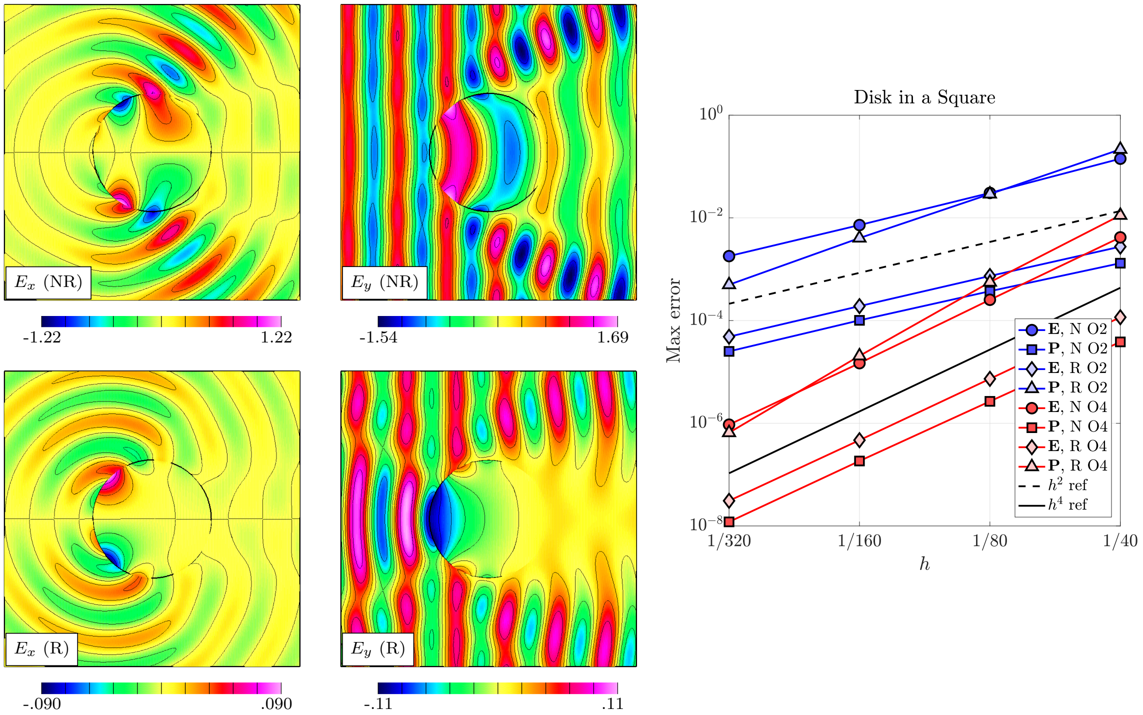

Figure 10: Left: Resonant (R) and non-resonant (NR) modes for scattering from a disk. Contours of the solution at $t = 0.3$ on grid $\mathcal{G}_d^{(8)}$. Right: Max-norm errors as a function of grid spacing for a resonant(R) and non-resonant (NR) modes.

Figure 10 compares contours of the solution components between the non-resonant (NR) and resonant (R) modes. The wave numbers of the two modes are chosen to be the same, but the variations in time, as determined by a root s of the dispersion relation, are significantly different. The R mode moves more slowly than the NR mode and is more strongly damped in time. The resonant mode, which is more strongly damped within the disk, exhibits a strong shadow region behind the disk.

Figure 10 also shows graphs of the max-norm errors at time $t = 0.5$ as a function of the grid-spacing for the second-order accurate and fourth-order accurate schemes. Results are shown for R and NR modes. Errors reported for a vector such as $\mathbf{E}$ denote the maximum error over all components of $\mathbf{E}$ and over all grid-points. The graphs clearly show that the numerical solutions are converging at very close to the predicted rates for both $\mathbf{E}$ and $\mathbf{P}$. As expected, the errors in the fourth-order accurate solution become much smaller than those for the second-order accurate solution as the mesh is refined.

6.3. Scattering from a dispersive dielectric sphere

In this section we compute the solution to the scattering of a plane wave passing through one dispersive material and scattering from a sphere of a different dispersive material. The exact solution has the same form as for non-dispersive materials [24] except that the series solution involves spherical Bessel functions with complex arguments.

The computational domain for the problem, as shown in Figure 11, is taken to be the region interior to the cube $[-2, 2]^3$, and it includes a spherical interface separating the two different dispersive materials. The spherical interface is centered at the origin and has radius equal to one.

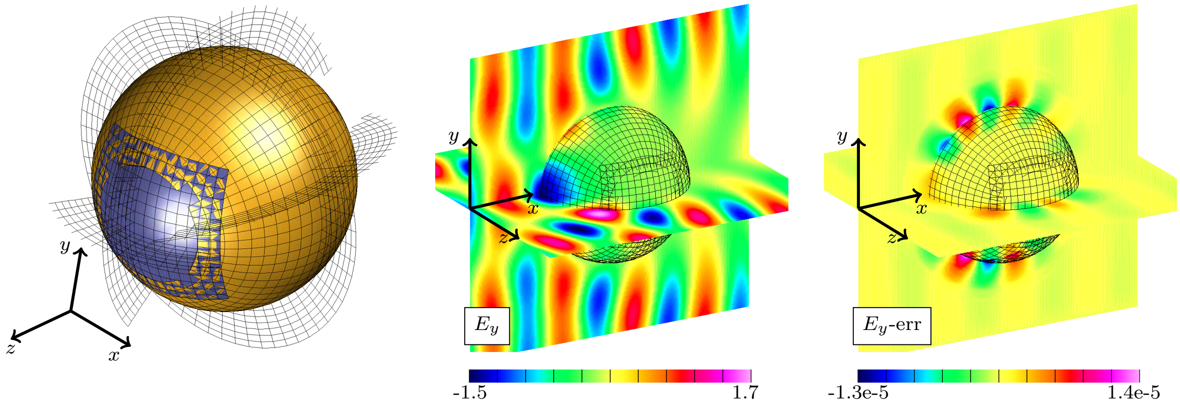

Figure 11: Left: a portion of the composite grid for scattering from a dispersive dielectric sphere. The region adjacent to the sphere is covered by three overlapping patches exterior to the sphere and another three on the interior (not shown). Middle and right: Contours of E_y and the error in E_y from the computed solution on grid $\mathcal{G}_s^{(8)}$ at $t = 0.5$. Coarsened versions of the grids on the surface of the sphere are also shown for reference.

The composite overlapping grid for this geometry consists of eight component grids. There are four grids in the region exterior to the spherical interface: a background Cartesian grid together with three interface-fitted patches that form a spherical shell. These later three component grids consist of a spherical polar patch covering most of the sphere and two orthographic patches over the two polar regions (see left plot of Figure 11). The orthographic patches remove the singularities at the two coordinate poles of the spherical-polar grid patch. The region inside the sphere is similarly covered with four component grids: an interior Cartesian grid togther with three patches that form a spherical shell fitted to the interior side of the interface.

The boundary conditions on the outer boundary are taken from the exact solution. The initial conditions are also assigned from the exact solution. The ghost points on either side of the spherical interface treated using our new discrete interface conditions. The outer domain is taken as a dispersive material with one polarization vector, while region inside the sphere is a dispersive material with two polarization vectors. The relevant parameters for the exact solution are $k = 2\pi$ and

Material	ϵ_0	N_p	$a_{0,m}$	$a_{1,m}$	$b_{0,m}$	$b_{1,m}$
outer	1	1	[1]	[0.1]	[1]	[0.2]
inner	2	2	[1.2, 1.4]	[0.1, 0.15]	[0.8, 1.2]	[0.05, 0.09]
NR-mode: $s = (-0.053776, -6.36236)$						
R-mode: $s = (-0.0982242, -0.982812)$						

Figure 11 shows contours of the computed solution for E_y at $t = 0.5$ for the resonant mode. It is noted that the tangential components of the electric field are continuous at the interface while the normal components jump, and thus E_y is discontinuous at the interface except where the surface of the sphere is tangent to the y-axis. The errors in E_y are also plotted and these are small and reasonably smooth in each domain indicating no obvious artifacts from either the interface conditions or interpolation between component grids. A grid resolution study is performed on a sequence of composite grids of increasing resolution. The composite grid with grid spacing approximately equal to $\Delta s^{(\ell)} = 1/(10\ell)$ is denoted by $\mathcal{G}_s^{(\ell)}$. Maximum-norm error convergence results are shown in Figure 12 for the second-order accurate and fourth-order accurate approximations. Results are

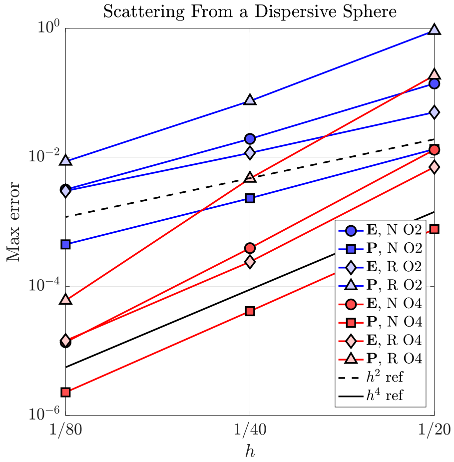

Figure 12: Maximum errors versus grid spacing for scattering of a dispersive plane wave from a dispersive solid sphere. Results are shown for the second-order acccurate scheme (in blue) and the fourth-order accurate scheme (in red). Errors for a non-resonant mode (N) and a resonant mode (R) are given.

shown for a resonant (R) and non-resonant (NR) mode. The graphs clearly show that the numerical solutions are converging at close to the predicted rates for both **E** and **P**. As before, the errors in the fourth-order accurate solution become much smaller than those for the second-order accurate solution as the mesh is refined.

6.4. Scattering from a multi-material disk

To demonstrate the accuracy, flexibility and robustness of the CgMx simulation code with the new interface approximations, we consider a scattering problem involving several different dispersive materials separated by numerous curved interfaces as shown in Figure 13. A traveling wave with Gaussian cross-section moves from left to right, and it scatters from a collection of dispersive disks. A self-convergence study is performed to show the estimated convergence rates for solutions of this complex problem at different grid resolutions.

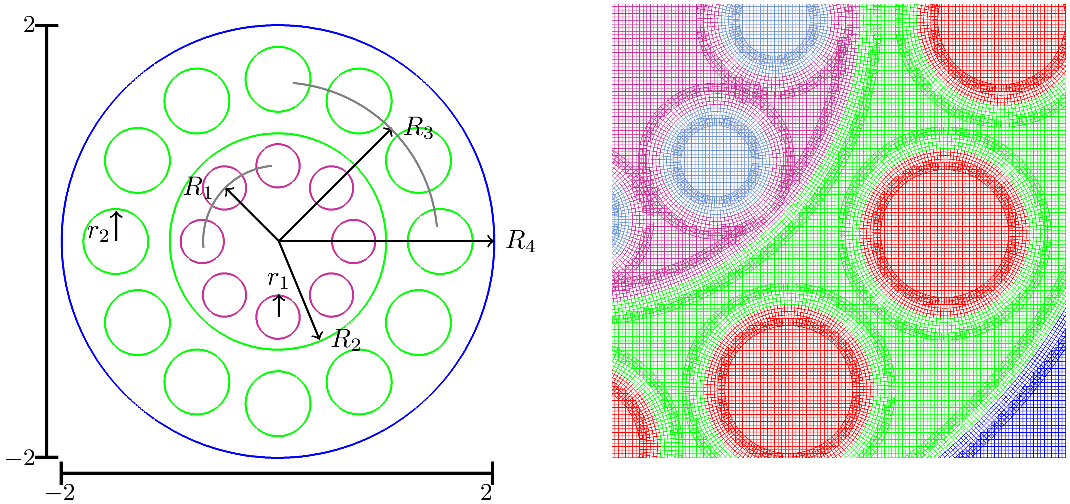

Figure 13: Left: Geometry for the multi-domain scattering example. Right: Enlarged view of the composite grid with different material regions coded by their colours.

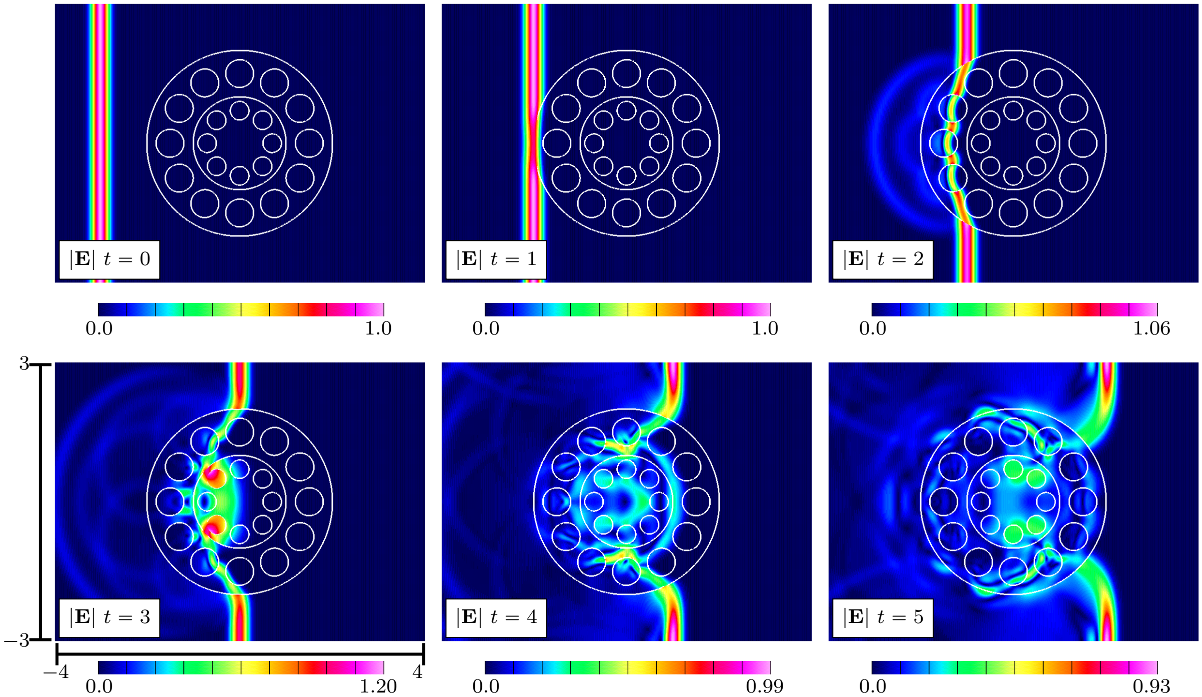

Figure 14: A Gaussian traveling-wave scattering from the multi-disk structure. Contours of $|\mathbf{E}|$ at selected times.

The composite grid for the geometry, as shown in Figures 2 and 13, is denoted by $\mathcal{G}_{\rm md}^{(\ell)}$ and has grid spacing approximately equal to $\Delta s^{(\ell)} = 1/(10\ell)$. The material disks are enclosed in a large rectangle with dimensions $[-4,4]\times[-3,3]$. An inner circular region of radius $R_2 = 1$ contains eight small disks each of radius $r_1 = 0.2$, which are equally spaced around a circle of radius $R_1 = 0.7$. An annular region of outer radius $R_4 = 2$ surrounds the inner disk and contains twelve disks of radius $r_2 = 0.3$ arranged along a circle of radius $R_3 = 1.5$. As shown in Figure 13, each domain has a background Cartesian grid together with a narrow annular grid fitted to each curved interface.

The initial conditions are taken to match a traveling wave with Gaussian profile, initially centered at $x_0 = -3$, and given by

$$H_z(x,y,t) = \exp\left[-\beta\big(k_x(x-x_0) + k_y(y-y_0) - \omega t\big)^2\right], \tag{91a}$$

$$E_x(x,y,t) = \frac{k_y}{\epsilon_0\omega} H_z(x,y,t), \tag{91b}$$

$$E_y(x,y,t) = \frac{-k_x}{\epsilon_0\omega} H_z(x,y,t), \tag{91c}$$

where we take $\epsilon_0 = 1$, $k_x = 0.5$, $k_y = 0$, $\beta = 120$ and $\omega = 0.5$. The solutions at $t = 0$ and $t = -\Delta t$ are set from (91) as initial conditions for the scheme. The boundary conditions on top and bottom of the rectangular outer domain are taken as periodic, and far-field boundary conditions are used on the left and right faces.

The parameters for the material in the outer domain and the materials that make up the scatterer, identified by the colours of the grids that appear in Figures 2 and 13, are taken as follows:

Material	ϵ_0	N_p	$a_{0,m}$	$a_{1,m}$	$b_{0,m}$	$b_{1,m}$
outer (blue)	1	0				
green	2	1	$[0.7]$	$[0]$	$[6]$	$[0.2]$
red	4	3	$[0.9, 0.8, 0.7]$	$[0.1, 0.08, 0.06]$	$[4, 3, 2]$	$[0.05, 0.07, 0.09]$
purple	0.5	2	$[1.1, 0.6]$	$[0, 0.05]$	$[3, 1.5]$	$[0.1, 0.2]$
light blue	0.25	1	$[0.8]$	$[0.05]$	$[2]$	$[0.05]$

To estimate the accuracy of the computed solution, self-convergence tests for the second-order and fourth-order accurate schemes are performed and the results are presented in Table 1. Solutions are computed on the composite grids $\mathcal{G}^{(\ell)}_{\rm md}$, $\ell = 2$, 4 and 8. The maximum error $\mathcal{E}^{\kappa}_{\ell}$ in the solution component κ for grid $\mathcal{G}^{(\ell)}_{\rm md}$, and the corresponding convergence rate, are estimated using a Richardson extrapolation procedure following the approach described in [25]. The results in the table show that the max-norm errors are converging at close to second-order for the second-order accurate scheme and close to fourth-order for the fourth-order accurate scheme.

Multiple disks, second-order				
$\Delta s^{(\ell)}$	$\mathcal{E}^{(E_s)}_{\ell}$	r	$\mathcal{E}^{(E_y)}_{\ell}$	r
1/20	2.6e-2		2.8e-2	
1/40	6.2e-3	4.1	6.6e-3	4.3
1/80	1.5e-3	4.1	1.5e-3	4.3
rate		2.05		2.11

Multiple disks, fourth-order				
$\Delta s^{(\ell)}$	$\mathcal{E}^{(E_s)}_{\ell}$	r	$\mathcal{E}^{(E_y)}_{\ell}$	r
1/20	3.5e-4		5.0e-4	
1/40	2.0e-5	17.3	3.0e-5	16.6
1/80	1.2e-6	17.3	1.8e-6	16.6
rate		4.11		4.05

Table 1: Max-norm self-convergence results for scattering from multiple disks at $t = 3$. The column labeled “r” denotes the ratio of the errors. The convergence rates estimated by Richardson extrapolation are close to the expected rates.

7. Conclusions

A high-order accurate finite-difference scheme for solving the dispersive time-domain Maxwell’s equations with a generalized and material interfaces was described. A generalized dispersion material model (GDM) was used to model general linear dispersive effects together with auxilary differential equations (ADE) to model the polarization vectors. Composite overlapping grids were used to treat complex geometry with boundary and interface conforming grids. The time-stepping was based on three-level single-stage schemes for Maxwell’s equations in second-order form, which achieve high-order accuracy in space and equal-order accuracy in time. Interface conditions based on compatibility conditions were developed for second-order accurate and fourth-order accurate versions of the scheme. An interface projection based on a Riemann problem was developed. This approach to interfaces was found to retain the large CFL-one time-step restriction associated with the interior schemes. One key result of the paper was showing how to treat the polarization terms that appear in the interface compatibility conditions so as to retain the three-level and centered nature of the approximation. The approach was based on taking a virtual step on the interface to the next time. The second-order scheme was embedded in a hierarchial fashion within the fourth-order scheme. A second key result, applicable to a more general class of problems, was a showing how to solve the resulting coupled interface conditions for the fourth-order scheme in a locally decoupled manner and thus avoiding the solution of large coupled system of equations on the interface.

Here the second-order accurate scheme was used to approximate some mixed derivative terms that appear in the fourth-order accurate interface conditions.

The stability of the new schemes were studied using model problem analysis. A semi-discrete analysis of a one-dimensional interface problem (discretized in space with time kept continuous) showed that the coupled problem for the second-order accurate scheme with discrete interface conditions was stable provided the schemes on each sub-domain were stable. A matrix stability analysis confirmed the stability of the second-order accurate and fourth-order accurate schemes for the fully-discrete model problem .

The new schemes were carefully verified for the case of a planar interface between dispersive materials in two and three space dimensions, the scattering from two-dimensional disk and the scattering from a three-dimensional sphere. Exact solutions for the dispersive Maxwell equations were developed for all these cases. The schemes were found to be accurate and stable. A final complex example showed the scattering of a Gaussian travelling wave from a collection of many materials regions. A self-convergence grid-refinement study confirmed the accuracy of the schemes.

Appendix A. Details required to complete the proof of Theorem 4

We prove that, under the assumptions of Theorem 4, there are no solutions to (86) for $\text{Re}(s) > 0$. Using $z_\xi = \lambda_\xi^2 h_\xi^2 = \frac{h_\xi^2}{c_\xi^2} s^2(1+\chi_\xi)$ from (83) and substituting into the factors $\sqrt{z_\xi}$ in (86) leads to the equivalent condition

$$\frac{1}{c_L \mu_{0,L}} \sqrt{1+\chi_L}\sqrt{1+z_L/4} = -\frac{1}{c_R \mu_{0,R}} \sqrt{1+\chi_R}\sqrt{1+z_R/4}, \tag{A.1}$$

after cancelling factors of s on both sides. Our focus now is on showing that (A.1) has no solutions for $\text{Re}(s) > 0$. We start with a lemma.

Lemma 1. *If the GDM coefficients satisfy* (58) *and if* $\text{Re}(s) > 0$*, then*

$$\text{Im}(s)\,\text{Im}(\chi) \leqslant 0.$$

Proof. From (59), the imaginary parts of χ_m and s satisfy

$$\text{Im}(s)\text{Im}(\chi_m) = -\Big(a_{1,m}|s|^2 + (a_{0,m}b_{1,m} - a_{1,m}b_{0,m}) + 2a_{0,m}\text{Re}(s)\Big)\frac{\text{Im}(s)^2}{d_m}. \tag{A.2}$$

Thus, if the conditions in (58) hold and $\text{Re}(s) > 0$, then (A.2) implies

$$\text{Im}(s)\,\text{Im}(\chi_m) \leqslant 0. \tag{A.3}$$

Summing (A.3) gives

$$\text{Im}(s)\,\text{Im}(\chi) \leqslant 0,$$

which completes the proof of the lemma. □

The proof that (A.1) has no solutions for $\text{Re}(s) > 0$ is split into different cases, and in each case we show that the argument of the complex variable on the left-hand side of (A.1) cannot equal that on the right-hand side. The first major choice is on the sign of $\mathrm{Im}(s)$ so that we may use Lemma 1. We first choose $\mathrm{Im}(s) \geqslant 0$ which implies $\mathrm{Im}(\chi_\xi(s)) \leqslant 0$ from Lemma 1. The proof for the second major choice of $\mathrm{Im}(s) \leqslant 0$ and $\mathrm{Im}(\chi_\xi(s)) \geqslant 0$ follows in a similar way to that given below, and is not given here.

Introduce the polar form for the complex quantities s, $\sqrt{1+\chi_\xi}$ and z_ξ, and use $\mathrm{Re}(s) > 0$, $\mathrm{Im}(s) \geqslant 0$, $\mathrm{Im}(\chi_\xi(s)) \leqslant 0$ and $\mathrm{Re}(\lambda_\xi) \neq 0$ to define bounds on their arguments. We have

$$s = re^{i\theta}, \qquad 0 \leqslant \theta < \pi/2, \tag{A.4a}$$

$$\sqrt{1+\chi_\xi} = \rho_\xi e^{i\phi_\xi}, \qquad -\pi/2 \leqslant \phi_\xi \leqslant 0, \tag{A.4b}$$

$$z_\xi = \frac{h_\xi^2}{c_\xi^2}\,\lambda_\xi^2 = \frac{h_\xi^2}{c_\xi^2}\,s^2(1+\chi_\xi) = \tilde{R}_\xi e^{i\,2(\theta+\phi_\xi)}, \qquad -\pi < 2(\theta+\phi_\xi) < \pi, \tag{A.4c}$$

where r, ρ_ξ and $\tilde{R}_\xi$ are their respective magnitudes, and θ, ϕ_ξ and $\mathrm{Arg}(z_\xi) = 2(\theta+\phi_\xi)$ are their arguments. Here, $\mathrm{Arg}(w)$ denotes the principal value of the argument of the generic complex variable w. Note that we exlude $\mathrm{Arg}(z_\xi) = \pi$ in (A.4c), since $\mathrm{Re}(\lambda_\xi) \neq 0$. Also, it should be kept in mind that the prinicpal branch is used for all square root functions.

Define

$$H_\xi \overset{\text{def}}{=} \frac{1}{c_\xi\,\mu_{0,\xi}}\sqrt{1+\chi_\xi}\sqrt{1+z_\xi/4},$$

which is the quantity that appears on the left and right-hand sides of (A.1). Our goal, then, is to show there are no solutions of $H_L = -H_R$ for $\mathrm{Re}(s) > 0$. There is a special case, where $H_L = H_R = 0$, which implies $\chi_\xi = -1$ or $z_\xi = -4$. When $z_\xi = -4$, λ_ξ is pure imaginary which contradicts our assumption $\mathrm{Re}(\lambda_\xi) \neq 0$. When $\chi_\xi = -1$, $\lambda_\xi = 0$ which is again a contradiction. Therefore we can exclude the case $H_L = H_R = 0$. For the remaining cases, it is helpful to note that the argument of $\sqrt{1+z_\xi/4}$ appearing in (A.1) can be bounded by the argument of $\sqrt{z_\xi}$ as follows:

$$\mathrm{Arg}(\sqrt{1+z_\xi/4}) \leqslant \mathrm{Arg}(\sqrt{z_\xi}), \qquad \text{for } 0 \leqslant \mathrm{Arg}(z_\xi) < \pi,$$

$$\mathrm{Arg}(\sqrt{1+z_\xi/4}) \geqslant \mathrm{Arg}(\sqrt{z_\xi}), \qquad \text{for } -\pi < \mathrm{Arg}(z_\xi) \leqslant 0.$$

The remainder of the proof is divided into three cases depending on the sign of $\mathrm{Im}(z_\xi)$.

Case I: Assume $\mathrm{Im}(z_\xi) \geqslant 0$ for $\xi = L, R$, so that $0 \leqslant 2(\theta+\phi_\xi) < \pi$, then

$$\sqrt{1+z_\xi/4} = \hat{R}_\xi e^{i\hat{\theta}_\xi}, \qquad 0 \leqslant \hat{\theta}_\xi \leqslant \theta+\phi_\xi < \pi/2,$$

which implies

$$\sqrt{1+\chi_\xi}\sqrt{1+z_\xi/4} = \rho_\xi\hat{R}_\xi e^{i(\phi_\xi+\hat{\theta}_\xi)}, \qquad -\pi/2 \leqslant \phi_\xi+\hat{\theta}_\xi \leqslant \theta+2\phi_\xi < \pi/2.$$

Thus, $-\pi/2 \leqslant \mathrm{Arg}(H_\xi) < \pi/2$ and H_ξ lies in the right-half plane (excluding the positive imaginary axis) for $\xi = L, R$, which implies that the only way for $H_L = -H_R$ to hold is for $H_\xi = 0$, but we have shown this is not possible either. Therefore there are no solutions to (A.1) for Case I.

Case II: Assume $\mathrm{Im}(z_\xi) \leqslant 0$ for $\xi = L, R$, so that $-\pi < 2(\theta + \phi_\xi) \leqslant 0$, then

$$\sqrt{1 + z_\xi/4} = \hat{R}_\xi e^{i\hat{\theta}_\xi}, \qquad -\pi/2 < \theta + \phi_\xi \leqslant \hat{\theta}_\xi < 0,$$

which implies

$$\sqrt{1 + \chi_\xi}\sqrt{1 + z_\xi/4} = \rho_\xi \hat{R}_\xi e^{i(\phi_\xi + \hat{\theta}_\xi)}, \qquad -\pi < \theta + 2\phi_\xi \leqslant \phi_\xi + \hat{\theta}_\xi \leqslant 0.$$

Thus, $-\pi < \mathrm{Arg}(H_\xi) \leqslant 0$ and H_ξ lies in the lower half plane (excluding the negative real axis) for $\xi = L, R$ which again implies (A.1) has no solutions.

Case III: The third case is when $\mathrm{Im}(z_L)$ and $\mathrm{Im}(z_R)$ are of opposite signs. Without loss of generality we may take $\mathrm{Im}(z_L) \geqslant 0$ and $\mathrm{Im}(z_R) < 0$. Note that from the polar form for z_ξ in (A.4c) we must have $\phi_R < \phi_L$ for this case to apply. From $\mathrm{Im}(z_L) \geqslant 0$ and $\mathrm{Im}(z_R) < 0$, and using the results from Cases I and II, it follows that

$$\begin{aligned} \sqrt{1 + \chi_L}\sqrt{1 + z_L/4} &= \rho_L \hat{R}_L e^{i(\phi_L + \hat{\theta}_L)}, \qquad && -\pi/2 \leqslant \phi_L + \hat{\theta}_L \leqslant \theta + 2\phi_L < \pi/2, \\ \sqrt{1 + \chi_R}\sqrt{1 + z_R/4} &= \rho_R \hat{R}_R e^{i(\phi_R + \hat{\theta}_R)}, \qquad && -\pi < \theta + 2\phi_R \leqslant \phi_R + \hat{\theta}_R \leqslant 0. \end{aligned} \tag{A.5a}$$

Multiplying the second expression by $-1 = e^{i\pi}$ adds π to the angle, so that

$$-\sqrt{1 + \chi_R}\sqrt{1 + z_R/4} = \rho_R \hat{R}_R e^{i(\phi_R + \hat{\theta}_R + \pi)}, \qquad 0 < \theta + 2\phi_R + \pi \leqslant \phi_R + \hat{\theta}_R + \pi \leqslant \pi \tag{A.5b}$$

Unfortunately, the ranges for $\mathrm{Arg}(H_L)$ and $\mathrm{Arg}(-H_R)$ given in (A.5) overlap and so we need a more refined argument. Note that from $-\pi/2 \leqslant \phi_\xi \leqslant 0$ and $\phi_R < \phi_L$, it follows that

$$0 \leqslant \phi_L - \phi_R \leqslant \pi/2,$$

which implies

$$\theta + 2\phi_L \leqslant \theta + 2\phi_R + \pi. \tag{A.6}$$

Since $\mathrm{Arg}(H_L) = \phi_L + \hat{\theta}_L$ and $\mathrm{Arg}(-H_R) = \phi_R + \hat{\theta}_R + \pi$, it now follows from (A.5) and (A.6) that

$$\mathrm{Arg}(H_L) = \phi_L + \hat{\theta}_L \leqslant \theta + 2\phi_L \leqslant \theta + 2\phi_R + \pi \leqslant Arg(-H_R) = \phi_R + \hat{\theta}_R + \pi. \tag{A.7}$$

Therefore $\mathrm{Arg}(H_L) \leqslant \mathrm{Arg}(-H_R)$. We must rule out the case $\mathrm{Arg}(H_L) = \mathrm{Arg}(-H_R)$. By assumption, $\mathrm{Im}(z_R) < 0$ so that $-\pi < \mathrm{Arg}(z_R) < 0$, which implies $\mathrm{Arg}(\sqrt{1 + z_R/4})$ is strictly greater than $\mathrm{Arg}(\sqrt{z_R})$. This implies $\theta + 2\phi_R + \pi < \mathrm{Arg}(-H_R)$ in (A.7). Therefore, $\mathrm{Arg}(H_L) < \mathrm{Arg}(-H_R)$ and so $H_L = -H_R$ is not possible.

We have thus shown that there are no solutions to the discrete interface condition in (86) with $\mathrm{Re}(s) > 0$, which completes the proof of Theorem 4.

References

[1] N. Kinsey, M. Ferrera, V. M. Shalaev, A. Boltasseva, Examining nanophotonics for integrated hybrid systems: a review of plasmonic interconnects and modulators using traditional and

alternative materials [Invited], J. Opt. Soc. Am. B 32 (1) (2015) 121–142.

[2] T. Ito, O. Slezak, M. Yoshita, H. Akiyama, Y. Kobayashi, High-precision group-delay dispersion measurements of optical fibers via fingerprint-spectral wavelength-to-time mapping, Photon. Res. 4 (1) (2016) 13–16.

[3] T. J. Kippenberg, A. L. Gaeta, M. Lipson, M. L. Gorodetsky, Dissipative Kerr solitons in optical microresonators, Science 361 (6402).
URL

[4] M. Miscuglio, A. Mehrabian, Z. Hu, S. I. Azzam, J. George, A. V. Kildishev, M. Pelton, V. J. Sorger, All-optical nonlinear activation function for photonic neural networks [Invited], Opt. Mater. Express 8 (12) (2018) 3851–3863.

[5] P. Minzioni, C. Lacava, T. Tanabe, J. Dong, X. Hu, G. Csaba, W. Porod, G. Singh, A. E. Willner, A. Almaiman, V. Torres-Company, J. Schröder, A. C. Peacock, M. J. Strain, F. Parmigiani, G. Contestabile, D. Marpaung, Z. Liu, J. E. Bowers, L. Chang, S. Fabbri, M. R. Vázquez, V. Bharadwaj, S. M. Eaton, P. Lodahl, X. Zhang, B. J. Eggleton, W. J. Munro, K. Nemoto, O. Morin, J. Laurat, J. Nunn, Roadmap on all-optical processing, Journal of Optics 21 (6) (2019) 063001.
URL

[6] H. Zhang, L. Zhou, L. Lu, J. Xu, N. Wang, H. Hu, B. M. A. Rahman, Z. Zhou, J. Chen, Miniature multilevel optical memristive switch using phase change material, ACS Photonics 6 (9) (2019) 2205–2212.

[7] J. Duan, Y. Li, Y. Zhou, Y. Cheng, J. Chen, Near-field optics on flatland: from noble metals to van der waals materials, Advances in Physics: X 4 (1) (2019) 1593051.

[8] I.-H. Lee, D. Yoo, P. Avouris, T. Low, S.-H. Oh, Graphene acoustic plasmon resonator for ultrasensitive infrared spectroscopy, Nature Nanotechnology 14 (4) (2019) 313.

[9] D. K. Gramotnev, S. I. Bozhevolnyi, Nanofocusing of electromagnetic radiation, Nature Photonics 8 (1) (2014) 13.

[10] S. Lian, L. J. Prokopeva, H. Chen, A. V. Kildishev, Designing optimal nanofocusing with a gradient hyperlens, Nanophotonics 7 (2) (2018) 479.

[11] L. J. Prokopeva, J. D. Borneman, A. V. Kildishev, Optical dispersion models for time-domain modeling of metal-dielectric nanostructures, IEEE Transactions on Magnetics 47 (2011) 1150–1153.

[12] J. Angel, J. W. Banks, W. D. Henshaw, M. J. Jenkinson, A. V. Kildishev, G. Kovačič, L. J. Prokopeva, D. W. Schwendeman, A high-order accurate scheme for Maxwell's equations with a generalized dispersion model, J. Comput. Phys. 378 (2019) 411–444.

[13] K. S. Yee, Numerical solution of initial boundary value problems involving Maxwell's equations in isotropic media, IEEE Transactions on Antennas and Propogation 14 (1966) 302–307.

[14] J. S. Hesthaven, High-order accurate methods in time-domain computational electromagnetics: A review, Advances in imaging and electron physics 127 (2003) 59–123.

[15] A. Taflove, S. C. Hagness, Computational Electrodynamics: The Finite-Difference Time-Domain Method, Artech House, 2000.

[16] G. C. Cohen, Higher-Order Numerical Methods for Transient Wave Equations, Springer, New York, 2002.

[17] H.-O. Kreiss, N. A. Petersson, J. Ystöm, Difference approximations for the second order wave equation, SIAM J. Numer. Anal. 40 (5) (2002) 1940–1967.

[18] C. A. Balanis, Advanced Engineering Electromagnetics, John Wiley & Sons, 1989.

[19] W. D. Henshaw, Ogen: An overlapping grid generator for Overture, Research Report UCRL-MA-132237, Lawrence Livermore National Laboratory (1998).

[20] W. D. Henshaw, A high-order accurate parallel solver for Maxwell's equations on overlapping grids, SIAM J. Sci. Comput. 28 (5) (2006) 1730–1765.

[21] G. S. Chesshire, W. D. Henshaw, Composite overlapping meshes for the solution of partial differential equations, J. Comput. Phys. 90 (1) (1990) 1–64.

[22] J. Angel, J. W. Banks, W. D. Henshaw, High-order upwind schemes for the wave equation on overlapping grids: Maxwell's equations in second-order form, J. Comput. Phys. 352 (2018) 534–567.

[23] J. W. Banks, W. D. Henshaw, Upwind schemes for the wave equation in second-order form, J. Comput. Phys. 231 (17) (2012) 5854–5889.

[24] H. C. van de Hulst, Light Scattering by Small Particles, Dover Publications, Inc., 1957.

[25] W. D. Henshaw, D. W. Schwendeman, Parallel computation of three-dimensional flows using overlapping grids with adaptive mesh refinement, J. Comput. Phys. 227 (16) (2008) 7469–7502.